# Probing the exciton condensate phase in 1T-TiSe2 with photoemission

Claude Monney, Eike Schwier, Michael Gunnar Garnier, N. Mariotti, Clement Didiot, Hervé Cercellier, Jacques Marcus, Helmut Berger, A.N. Titov, Hans Beck, et al.

New Journal of Physics
The open-access journal for physics

# Probing the exciton condensate phase in 1*T*-$TiSe_2$ with photoemission

**C Monney[1,6], E F Schwier[1], M G Garnier[1], N Mariotti[1], C Didiot[1], H Cercellier[2], J Marcus[2], H Berger[3], A N Titov[4,5], H Beck[1] and P Aebi[1,7]**

[1] Département de Physique and Fribourg Center for Nanomaterials, Université de Fribourg, CH-1700 Fribourg, Switzerland
[2] Institut Néel, CNRS-UJF, BP 166, 38042 Grenoble, France
[3] EPFL, Institut de Physique de la Matière Condensée, CH-1015 Lausanne, Switzerland
[4] Institute of Metal Physics UrD RAS, Ekaterinburg 620219, Russia
[5] Institute of Metallurgy UrD RAS, Amundsen St. 101, Ekaterinburg 620016, Russia
E-mail: philipp.aebi@unifr.ch

*New Journal of Physics* **12** (2010) 125019 (31pp)
Received 13 May 2010
Published 22 December 2010
Online at http://www.njp.org/
doi:10.1088/1367-2630/12/12/125019

**Abstract.** We present recent results obtained using angle-resolved photoemission spectroscopy performed on 1*T*-$TiSe_2$. Emphasis is put on the peculiarity of the bandstructure of $TiSe_2$ compared to other transition metal dichalcogenides, which suggests that this system is an excellent candidate for the realization of the excitonic insulator phase. This exotic phase is discussed in relation to the BCS theory, and its spectroscopic signature is computed via a model adapted to the particular bandstructure of 1*T*-$TiSe_2$. A comparison between photoemission intensity maps calculated with the spectral function derived for this model and experimental results is shown, giving strong support for the exciton condensate phase as the origin of the charge density wave transition observed in 1*T*-$TiSe_2$. The temperature-dependent order parameter characterizing the exciton condensate phase is discussed, both on a theoretical and an experimental basis, as well as the chemical potential shift occurring in this system. Finally, the transport properties of 1*T*-$TiSe_2$ are analyzed in the light of the photoemission results.

[6] Present address: Swiss Light Source, Paul Scherrer Institut, CH-5232 Villigen PSI, Switzerland.
[7] Author to whom any correspondence should be addressed.

## Contents



## 1. Introduction

The *excitonic insulator phase* appeared in the mid-1960s as a theoretical prediction [1, 2]. In its simplest version, its basic ingredients are a single valence and a single conduction band, having a semimetallic or semiconductor configuration. Then, if the overlap or the gap between them is small enough, bound states of holes and electrons, called excitons, will condense in a macroscopic state and drive the system into a new ground state, provided the temperature is sufficiently low. A charge density wave (CDW) arises naturally from the coupling between the valence and conduction bands, opening a gap between them at low temperature (LT) and transforming the semimetallic or semiconducting configuration into an insulating one. In other words, the presence of condensed excitons in the system creates the CDW as a purely electronic process.

Among the collective phenomena at play in condensed matter, superconductivity is among the most interesting ones, not only for its perspectives on technology but also for its complexity and its variety. With the seminal work of Bardeen, Cooper and Schrieffer (BCS), a significant advance has been made in the understanding of this phenomenon. In the BCS theory of conventional superconductivity, the pairing interaction of electrons has proved to be not trivial. A delicate mixing of the Coulomb interaction with the dynamical screening effect of phonons is necessary to achieve the effect of overscreening, essential to transform the repulsive Coulomb interaction between two electrons into an attractive one, leading to the creation of Cooper pairs, the basic charged entity of conventional superconductivity.

In the case of the excitonic insulator phase, the situation is fundamentally reversed. The bare Coulomb interaction turns out to be already attractive between the electron and the hole, owing to their opposite charges, so that excitons can build up without the interplay of complicated physics. However, screening of the Coulomb interaction weakens the pairing interaction, leading to weakly bound excitons, and is unfavorable for the onset of the exciton

condensate. Excitons are neutral quasi-particles and are therefore undetectable in standard transport experiments, since their signature in such experiments is similar to that of a conventional insulator. For this reason, it is more difficult to reveal an excitonic insulator system than a superconducting one.

The transition metal dichalcogenides (TMDCs) form a large family of quasi-two-dimensional systems, composed of transition metal atoms and chalcogen atoms. Their atomic structure is made of layers of transition metal atoms, forming a triangular lattice, in prismatic or octahedral coordination with their neighboring chalcogen atoms. These layers are stacked along the $c$-direction and glued together by van der Waals forces. The chalcogen atom being in an $ns^2\ np^4$ electronic configuration ($n$ is the principal quantum number of the partially filled last shell), four electrons are taken away from the transition metal atom, in a purely ionic picture. This means that, for group IVA transition metals ($(n-1)d^2\ ns^2$ electronic configuration), the atom is left in a $d^0$ valence state, while for the group VA transition metals ($(n-1)d^3\ ns^2$), it is left in a $d^1$ configuration. However, this simple ionic picture does not hold in real TMDCs, since the nature of the bond is rather covalent [3]. In a real crystal, crystal field splitting and hybridization between the chalcogen and the transition metal orbitals will modify this situation. Nonetheless, the typical bandstructure of these systems can still be schematically described in a simplified picture, by the combination of a valence and a conduction band, whose relative position depends mainly on the period to which the atoms belong. Considering particular elements of the group IVA and VA transition metals, the situation can be summarized as in figure 1. For group IVA, we consider Ti atoms, in combination with S, Se and Te chalcogens. As mentioned above, in an ionic picture, Ti atoms are left in a $d^0$ valence state and the chalcogen has full subshells. Therefore, the bandstructure of the TMDC must be that of a compensated system (the hole density is equal to the electron density). Then, for the most electronegative chalcogen (S), a clear semiconducting configuration (figure 1(a)) is obtained in the pure $1T$-$TiS_2$ system [3]. This result is confirmed by recent photoemission data [4].

Going to the next chalcogen (Se), which is less electronegative, the electronic configuration (figure 1(b)) changes into that of a small gap semiconductor or a semimetal (the precise situation is still debated in the literature [5]–[8]). Finally, in the case of the chalcogen with the smallest electronegativity (Te), the system becomes metallic (figure 1(c)), with a large overlap between the valence and conduction bands [3, 9]. Shifting to the group VA, we consider the particular case of the transition metal Ta (which is less electronegative than Ti). Due to the extra electron coming from the d-subshell of Ta, in a first approximation, we expect the chemical potential to be shifted into the conduction band, leading to an uncompensated system. According to density functional theory (DFT), $1T$-$TaS_2$ displays already an overlap between the valence and conduction bands[8] (figure 1(d)) [10]. Moreover, as expected, the conduction band is now partially in the occupied states. In the case of $1T$-$TaSe_2$, the DFT bandstructure is similar to that of $1T$-$TaS_2$ with a larger overlap between the valence and conduction bands (figure 1(e)) [10]. Finally, when Se is replaced by Te, the $1T$ structure cannot be achieved. However, the $TaTe_2$ crystal structure is based on a monoclinic unit cell, such that it looks like a distorted $1T$ structure [11]. The corresponding electronic structure (figure 1(f)) can still be described in our simple approach with a large overlap between the valence and the conduction bands and with a valence band partially in the unoccupied states. Of course, this simple view on the electronic structure of some selected TMDCs may be dramatically changed by strong correlations.

[8] To simplify the comparison with the Ti-based compounds, we will still talk about a valence and a conduction band, although the system based on Ta is now metallic.

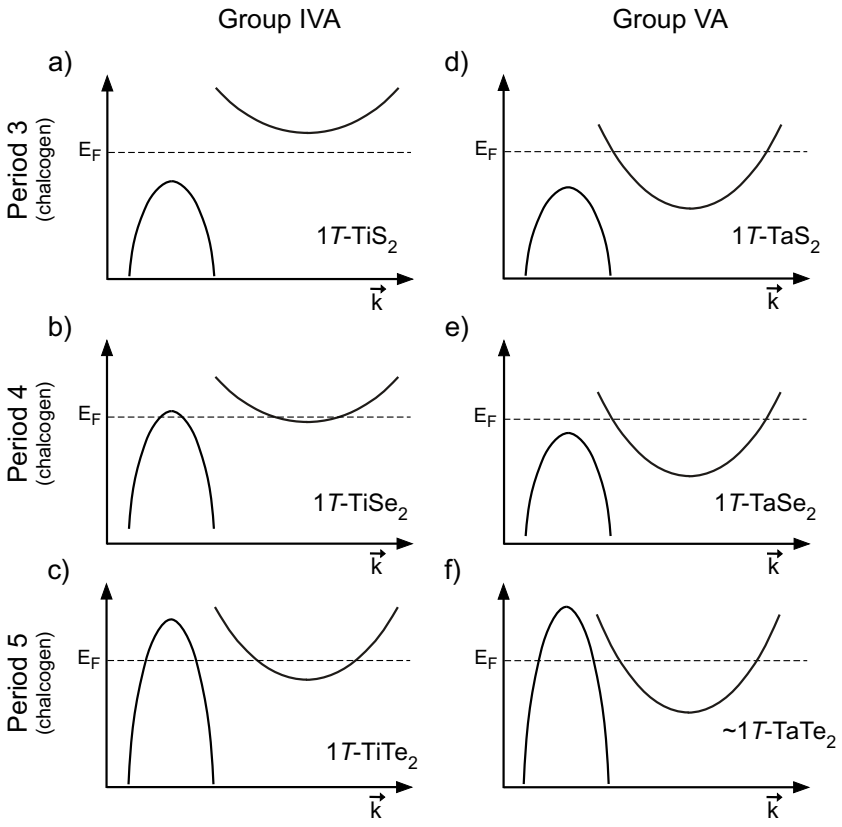


**Figure 1.** Schematic electronic configuration close to the Fermi energy of typical TMDCs. Hole-like and electron-like bands are of chalcogen p character and transition metal d character, respectively.

This simple comparison between the bandstructures of selected TMDCs will now help us to better understand the particular case of $1T$-$TiSe_2$. Indeed, among the stereotyped electronic structures discussed above, the one of $1T$-$TiSe_2$ stands out from the others due to the proximity of its band extrema to the Fermi energy ($E_F$). This has two main implications. Firstly, in opposition to semiconductors with a large gap, the bandstructure of $1T$-$TiSe_2$ (figure 1(b)) offers enough electronic states close to $E_F$, which can participate in collective phenomena with a low energy cost. In other words, we expect that the corresponding electronic susceptibility will be high for wave vectors connecting the two bands [12]. Secondly, in contrast to metallic systems, this configuration restrains the effect of screening, since the number of free charge carriers is limited. As explained above, the delicate balance between these two properties is essential for the possible realization of the excitonic insulator phase, making $1T$-$TiSe_2$ an excellent candidate for this exotic phase, as already proposed by Wilson 30 years ago [13, 14]. The electronic configuration is a little bit more complicated than displayed in figure 1(b). In fact, three symmetry equivalent conduction bands having their minima at the border of the Brillouin zone (BZ) (at the $L$ point, see figure 2(a)) are coupled to the valence band having its maximum at the center of the BZ (the $\Gamma$ point). For such a bandstructure, the main difference compared to the basic excitonic insulator phase is that the electron–hole coupling does not shift all the conduction bands away from the Fermi energy when opening a gap, leaving therefore

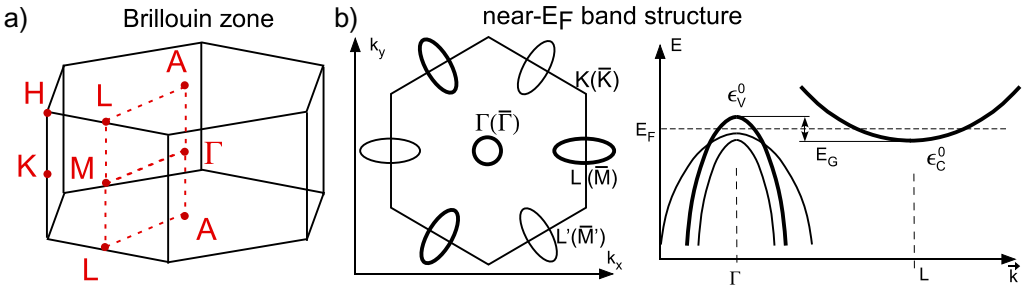


**Figure 2.** (a) BZ of $1T$-$TiSe_2$ with its high symmetry points. (b) Left: constant energy map near $E_F$ of $1T$-$TiSe_2$ in planes parallel to the $\Gamma MK$ plane, with electron pockets at $L(\bar{M})$ produced by the conduction band. In parentheses, the surface BZ notation is indicated for high symmetry points. Right: the valence bands have their maxima at $\Gamma$ and the conduction band has its minimum at $L$. In fact, there are three Se4p-derived bands at $\Gamma$. In our model, however, we will only consider the topmost one (thick black line).

unperturbed states close to the Fermi energy, which are reducing the insulating character of the transition [15]. As a consequence, we call this phase the *exciton condensate phase*. Furthermore, Zhitomirsky and Rice have shown that intervalley scattering (allowed in this three-conduction-band electronic configuration) increases the exciton binding energy, stabilizing thereby a dilute Bose gas of excitons [16]. More recently, stimulated by the possibility of an excitonic insulator phase in $TmSe_{0.45}Te_{0.55}$ [17], Fehske and co-workers investigated the phase diagram of the excitonic insulator phase with particular attention to the BCS–Bose–Einstein condensate (BEC) crossover, based on an effective mass model [18] and an extended Falicov–Kimball model (EFKM) [19, 20]. They also focused on the spectral signature of the BCS–BEC crossover in the EFKM [21].

Among the TMDCs, $1T$-$TiSe_2$ has stimulated much interest for 40 years, especially due to its commensurate $(2 \times 2 \times 2)$ CDW phase. At the critical temperature of $T_c \simeq 200\,\mathrm{K}$, this second-order phase transition is notably characterized by a peaking resistivity [22, 23] and a periodic lattice distortion (PLD) involving relatively small ionic displacements ($\leqslant 0.08\,\text{Å}$), accompanied by a phonon softening [24]. The electronic band structure and its elementary excitations have been measured with angle-resolved photoemission spectroscopy (ARPES). For recent experiments, see e.g. [5]–[8]. The bandstructure inferred at room temperature (RT) is schematically reproduced in figure 2(b), where the relative energy position of the valence and conduction bands is still controversial. At LT, intense backfolded bands, characteristic of the CDW phase, appear. As an alternative to the exciton condensate phase scenario, a band Jahn–Teller effect [25] has been proposed, supported by the fact that the PLD results in a tendency of the system to pass from the $1T$ (octhedral environment of the transition atom) to the $2H$ (prismatic environment) polytype. Nesting is not favored by the $1T$-$TiSe_2$ Fermi surface (FS) topology, since no large parallel portions of FS are present [26]. Recent calculations based on a one-dimensional model taking into account structural and excitonic charge fluctuations indicate that both phonons and excitons must underlie the CDW phase of $1T$-$TiSe_2$ [27].

In 2006, superconductivity was discovered in $TiSe_2$ intercalated with copper atoms, $Cu_xTiSe_2$ [28]. It was shown that Cu intercalation suppresses first the CDW phase and, at concentrations of $x \simeq 0.06$, a superconductive dome develops, reaching a maximum critical

temperature of 4.15 K at $x = 0.08$. The corresponding phase diagram is reminiscent of the one of the new iron pnictide superconductors. In this context, it is worth citing the recent work of Sawatzky *et al*, emphasizing that the pnictogen- and chalcogen-based materials are of particular interest, since these atoms possess high polarizability, which is, under certain circumstances, favorable to non-phonon-mediated superconductivity [29]. This polarizability can be seen as resulting from virtual excitonic fluctuations. It is then very tempting to suggest that such a mechanism may be at play in $Cu_xTiSe_2$. We close this discussion by mentioning that superconductivity under pressure has also been discovered in the pure $1T$-$TiSe_2$ compound, with again a very similar phase diagram [30].

After a short introduction to the general model of the excitonic insulator phase in section 2, general results of the BCS theory are first recalled and a typical BCS spectroscopic signature is shown in section 3. In section 4, this serves as a basis for a comparative discussion with the spectral function derived for the excitonic insulator phase calculated for a two-band electronic configuration. In section 5, the model is generalized to a four-band electronic configuration (from now on called the *exciton condensate phase*), which is more realistic for discussing the case of $1T$-$TiSe_2$. In this section, experimental data are also presented, showing very good agreement with the calculation, leading to strong support for the realization of the exciton condensate phase in $1T$-$TiSe_2$. In section 6, an order parameter with a mean-field-like temperature dependence is introduced in the model to study the corresponding temperature-dependent spectroscopic signature. This allows us then to discuss ARPES measurements performed over a wide temperature range, to extract the corresponding experimental order parameter and to recognize also a substantial chemical potential shift. Finally, in section 7, the transport properties of $1T$-$TiSe_2$ are discussed.

## 2. Description of the model

We give a brief summary of the main results of a previous theoretical work on the exciton condensate phase adapted to the electronic structure of $1T$-$TiSe_2$ [15], illustrated with the two-band excitonic insulator phase model.

We consider, in that model, electronic dispersions describing a single valence band $\epsilon_v(\vec{k})$ and three (one) conduction bands $\epsilon_c^i(\vec{k})$, $i = 1, 2, 3$ ($i = 1$).[9] The valence band is centered at $\Gamma$ and the conduction bands (mainly of Ti 3d character), equivalent by symmetry, are centered at the different $L$ points (at the $M$ point) of the BZ. The $\Gamma$ point is separated from the $L$ points by the spanning vectors $\vec{w}_i = \Gamma L$ ($\vec{w}_1 = \vec{w} = \Gamma M$).

The Hamiltonian of the model is composed of a one-electron part $H_0$ and a Coulomb interaction part $W$. The one-electron part contains the dispersions of the different bands

$$H_0 = \sum_{\vec{k}} \epsilon_v(\vec{k}) a^\dagger(\vec{k}) a(\vec{k}) + \sum_{\vec{k},i} \epsilon_c^i(\vec{k} + \vec{w}_i) b_i^\dagger(\vec{k}) b_i(\vec{k}).$$

Here $a^\dagger(\vec{k})$ and $b_i^\dagger(\vec{k})$ are operators creating electrons with wave vector $\vec{k}$ in the valence band and with wave vector $\vec{k} + \vec{w}_i$ in the conduction band labeled $i$, respectively.

[9] Without loss of generality, we keep the index $i$ for numbering the conduction bands, although it is useless in the case where only one conduction band is considered.

The interaction part $W$ contains only the direct Coulomb interaction between electrons in the valence and the conduction bands

$$W = \sum_{\vec{q},i} \rho_a(\vec{q}) V_c(\vec{q}) \rho^\dagger_{b,i}(\vec{q}, \vec{w}_i),$$

where we have introduced partial electron density operators

$$\rho_a(\vec{q}) = \sum_{\vec{k}} a^\dagger(\vec{k}+\vec{q}) a(\vec{k}), \quad \rho_{b,i}(\vec{q}, \vec{w}_i) = \sum_{\vec{k}} b^\dagger_i(\vec{k}+\vec{q}) b_i(\vec{k}).$$

In our calculation, only the Coulomb interaction between the valence and the conduction bands is considered. The Coulomb interaction potential is taken to be of the form (in three dimensions)

$$V_c(\vec{q}) = \frac{4\pi e^2}{\epsilon(\vec{q}) q^2}, \tag{1}$$

with $\epsilon$ being the dielectric function of the material. It must be emphasized here that the chemical potential is not included *ab initio* in the model, so that any change in the chemical potential resulting from the phase transition toward the excitonic insulator phase will not be calculated self-consistently. This issue will be addressed separately in section 6.

The Green's functions describing the valence band, $G_v(\vec{k}, t, t')$, and the conduction band labeled $i$, $G^i_c(\vec{k}, t, t')$, are defined according to

$$G_v(\vec{k}, t, t') = (-i)\langle T a(\vec{k}, t) a^\dagger(\vec{k}, t')\rangle,$$

$$G^i_c(\vec{k}, t, t') = (-i)\langle T b_i(\vec{k}, t) b^\dagger_i(\vec{k}, t')\rangle$$

($T$ denotes the time-ordering operator). They will be derived at the mean-field level in the sections below for different types of band structures.

## 3. Spectral function in the BCS theory

Before looking at the spectral function of the excitonic insulator phase, we make a short digression in the BCS theory of superconductivity and recall the analytical form of its spectral function. We cite here only the main results, since their derivations can be easily found in textbooks [31].

The typical BCS Hamiltonian has the form

$$H = \sum_{\vec{p}\sigma} \varepsilon(p) c^\dagger_\sigma(\vec{p}) c_\sigma(\vec{p}) + \frac{1}{2v} \sum_{\vec{q}\vec{p}\vec{p}'} \sum_{\sigma\sigma'} V(q) c^\dagger_\sigma(\vec{p}+\vec{q}) c^\dagger_{\sigma'}(\vec{p}'-\vec{q}) c_{\sigma'}(\vec{p}') c_\sigma(\vec{p}) \tag{2}$$

with an effective attractive interaction designed to model the phonon overscreened Coulomb interaction, with an attractive constant part up to the Debye frequency of the solid $\omega_D$

$$V(q) = \begin{cases} -V_0 & \text{for } |\varepsilon(q)| \leqslant \omega_D, \\ 0 & \text{otherwise.} \end{cases} \tag{3}$$

The fermionic operator $c_\sigma(\vec{p})$ creates an electron with momentum $\vec{p}$ and spin $\sigma$ in the band of (isotropic) dispersion $\varepsilon(p)$. This dispersion is such that near the Fermi energy it has linear behavior. However, a parabolic dispersion will be used here, which provides states

of momentum $-\vec{k}$ and $+\vec{k}$ necessary for building up Cooper pairs of zero center of mass momentum. The corresponding Green's functions are

$$\begin{aligned} G(\vec{p},\tau-\tau') &= -\langle T_\tau c_\sigma(\vec{p},\tau)c_\sigma^\dagger(\vec{p},\tau')\rangle, \\ F(\vec{p},\tau-\tau') &= -\langle T_\tau c_\downarrow(-\vec{p},\tau)c_\uparrow(\vec{p},\tau')\rangle, \\ F^\dagger(\vec{p},\tau-\tau') &= \langle T_\tau c_\uparrow^\dagger(\vec{p},\tau)c_\downarrow^\dagger(-\vec{p},\tau')\rangle, \end{aligned} \tag{4}$$

where $G$ is a standard Green's function and $F$ and $F^\dagger$ are called anomalous Green's functions, which are identically zero in the normal state.

We now recall directly their final form (in Matsubara frequency space)

$$\begin{aligned} G(\vec{p},\mathrm{i}p_n) &= -\frac{\mathrm{i}p_n+\varepsilon(p)}{p_n^2+\varepsilon(p)^2+\Delta(\vec{p})^2}, \\ F^\dagger(\vec{p},\mathrm{i}p_n) &= \frac{\Delta(\vec{p})}{p_n^2+\varepsilon(p)^2+\Delta(\vec{p})^2} = F(\vec{p},\mathrm{i}p_n). \end{aligned} \tag{5}$$

$\Delta(\vec{p})$ is the order parameter characterizing the superconductive phase. We immediately see that when $\Delta = 0$, the anomalous Green's functions vanish, as required by equation (4). The poles of these Green's functions are the renormalized dispersions, namely $E(\vec{p}) = \pm\sqrt{\varepsilon(p)^2+\Delta(\vec{p})^2}$, corresponding to the excitation energy of the system. It allows us to rewrite these Green's functions in expanded form:

$$\begin{aligned} G(\vec{p},\mathrm{i}p_n) &= \frac{u(\vec{p})^2}{\mathrm{i}p_n-E(\vec{p})}+\frac{v(\vec{p})^2}{\mathrm{i}p_n+E(\vec{p})}, \\ F^\dagger(\vec{p},\mathrm{i}p_n) &= -u(\vec{p})v(\vec{p})\left(\frac{1}{\mathrm{i}p_n-E(\vec{p})}-\frac{1}{\mathrm{i}p_n+E(\vec{p})}\right) = F(\vec{p},\mathrm{i}p_n), \end{aligned}$$

where the coherence factors $u(\vec{p})^2 = (1+\varepsilon(p)/E(\vec{p}))/2$ and $v(\vec{p})^2 = (1-\varepsilon(p)/E(\vec{p}))/2$ have been introduced. The spectral function of the system is obtained from the (normal) retarded Green's function, namely

$$A(\vec{p},\omega) = -\frac{1}{\pi}\mathrm{Im}\,G^{\mathrm{ret}}(\vec{p},\omega) = u(\vec{p})^2\delta(\omega-E(\vec{p}))+v(\vec{p})^2\delta(\omega+E(\vec{p})). \tag{6}$$

Figure 3(a) displays the renormalization of a parabolic dispersion (dashed line) in the BCS superconductive phase for an order parameter fixed at $\Delta = 0.05$ eV, as seen by photoemission. Near $E_\mathrm{F}$, a gap opens and separates the dispersion into two curved dispersions, carrying spectral weights (SWs) corresponding to $u(p)^2$ and $v(p)^2$. These SW functions are displayed in figure 3(b), their sum being normalized to one. The high SW is distributed on the parts of the renormalized dispersions that are closer to the non-renormalized ones. The gap measured in photoemission is twice the BCS gap function, $E_\mathrm{g} = 2\Delta$. The reason for this is that one cannot excite just one electron from the BCS ground state (where all electrons are bound into pairs) when destroying a Cooper pair, but one must excite two electrons, paying therefore at least $2\Delta$.

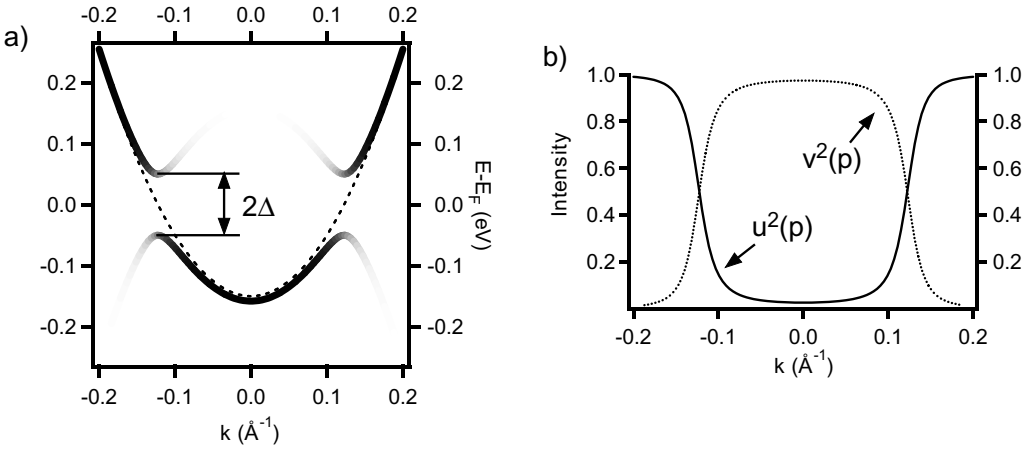


**Figure 3.** (a) Renormalized bands obtained with a bare parabolic dispersion (dashed line) in the BCS theory with the spectral function (equation (6)) for $\Delta = 0.05\,\mathrm{eV}$. Their SWs (given by $u(p)^2$ and $v(p)^2$), superimposed on the dispersions in grayscale coding, are plotted in graph (b).

## 4. The excitonic insulator phase (two bands)

We now proceed to the case of the excitonic insulator phase. For that purpose, we present in this section the spectral function calculated for a two-band electronic structure like that of figure 1(b), based on the theory shown in section 2. The dispersions are described by the following functions:

$$\epsilon_{\mathrm{v}}(\vec{k}) = \frac{\hbar^2\vec{k}^2}{2m_{\mathrm{v}}} + \epsilon_{\mathrm{v}}^0, \tag{7}$$

$$\epsilon_{\mathrm{c}}(\vec{k}) = \frac{\hbar^2(\vec{k}-\vec{w})^2}{2m_{\mathrm{c}}} + \epsilon_{\mathrm{c}}^0, \tag{8}$$

where the parameters have been chosen to be of the form $\varepsilon_{\mathrm{v}}^0 = 0.03\,\mathrm{eV}$, $\varepsilon_{\mathrm{c}}^0 = -0.04\,\mathrm{eV}$, $m_{\mathrm{v}} = -0.23m_{\mathrm{e}}$ and $m_{\mathrm{c}} = 5.5m_{\mathrm{e}}$ (similar to those in [15], but for a simpler band structure here).

We now give the results for the Green's functions of the valence and conduction bands without showing the details of their derivation. This is a mean-field calculation very similar to what is done in BCS theory of superconductivity [31] (see chapter 3). Its application to the particular case of the two-band excitonic insulator can be found in [2, 32]. The Green's function of the valence band is

$$G_{\mathrm{v}}(\vec{p},z) = \frac{z-\varepsilon_{\mathrm{c}}(\vec{p}+\vec{w})}{(z-\varepsilon_{\mathrm{v}}(\vec{p}))(z-\varepsilon_{\mathrm{c}}(\vec{p}+\vec{w}))-|\Delta(\vec{p})|^2} = \frac{1}{z-\varepsilon_{\mathrm{v}}(\vec{p})-\frac{|\Delta(\vec{p})|^2}{z-\varepsilon_{\mathrm{c}}(\vec{p}+\vec{w})}}. \tag{9}$$

This particular form of $G_{\mathrm{v}}$ emphasizes immediately the role of the self-energy

$$\Sigma_{\mathrm{v}}(\vec{p},z) = \frac{|\Delta(\vec{p})|^2}{z-\varepsilon_{\mathrm{c}}(\vec{p}+\vec{w})},$$

which involves the conduction band (around its minimum) and is purely real.

The Green's function for the conduction band reads

$$G_{\mathrm{c}}(\vec{p},z)=\frac{z-\varepsilon_{\mathrm{v}}(\vec{p}-\vec{w})}{(z-\varepsilon_{\mathrm{c}}(\vec{p}))(z-\varepsilon_{\mathrm{v}}(\vec{p}-\vec{w}))-|\Delta(\vec{p})|^2}=\frac{1}{z-\varepsilon_{\mathrm{c}}(\vec{p})-\frac{|\Delta(\vec{p})|^2}{z-\varepsilon_{\mathrm{v}}(\vec{p}-\vec{w})}}. \tag{10}$$

Both the valence (equation (9)) and the conduction (equation (10)) Green's functions have the same denominator (up to a shift of $\vec{w}$)

$$D(\vec{p},z)=(z-\varepsilon_{\mathrm{v}}(\vec{p}))(z-\varepsilon_{\mathrm{c}}(\vec{p}+\vec{w}))-|\Delta(\vec{p})|^2 \tag{11}$$

and its (real) roots are the renormalized dispersions in the condensate phase ($T<T_{\mathrm{c}}$), namely

$$\Omega_{\pm}(\vec{p})=\frac{1}{2}\left(\varepsilon_{\mathrm{v}}(\vec{p})+\varepsilon_{\mathrm{c}}(\vec{p}+\vec{w})\right)\pm\frac{1}{2}\sqrt{(\varepsilon_{\mathrm{v}}(\vec{p})-\varepsilon_{\mathrm{c}}(\vec{p}+\vec{w}))^2+4|\Delta(\vec{p})|^2}. \tag{12}$$

With these roots, the Green's functions can be decomposed into rational functions (involving only first-order poles) and their spectral functions can be computed:

$$\begin{aligned}A_{\mathrm{v}}(\vec{p},\Omega)&=u_{\mathrm{v}}^2(\vec{p})\delta(\Omega-\Omega_+(\vec{p}))+v_{\mathrm{v}}^2(\vec{p})\delta(\Omega-\Omega_-(\vec{p})),\\ A_{\mathrm{c}}(\vec{p},\Omega)&=u_{\mathrm{c}}^2(\vec{p})\delta(\Omega-\Omega_+(\vec{p}))+v_{\mathrm{c}}^2(\vec{p})\delta(\Omega-\Omega_-(\vec{p}))\end{aligned} \tag{13}$$

with the coherence factors being

$$\begin{aligned}u_{\mathrm{v}}^2(\vec{p})&=\frac{\Omega_+(\vec{p})-\varepsilon_{\mathrm{c}}(\vec{p}+\vec{w})}{\Omega_+(\vec{p})-\Omega_-(\vec{p})},\quad v_{\mathrm{v}}^2(\vec{p})=\frac{\Omega_-(\vec{p})-\varepsilon_{\mathrm{c}}(\vec{p}+\vec{w})}{\Omega_-(\vec{p})-\Omega_+(\vec{p})},\\ u_{\mathrm{c}}^2(\vec{p})&=\frac{\Omega_+(\vec{p})-\varepsilon_{\mathrm{v}}(\vec{p}-\vec{w})}{\Omega_+(\vec{p})-\Omega_-(\vec{p})},\quad v_{\mathrm{c}}^2(\vec{p})=\frac{\Omega_-(\vec{p})-\varepsilon_{\mathrm{v}}(\vec{p}-\vec{w})}{\Omega_-(\vec{p})-\Omega_+(\vec{p})}\end{aligned} \tag{14}$$

(satisfying $u_{\mathrm{v}}^2+v_{\mathrm{v}}^2=1$ and $u_{\mathrm{c}}^2+v_{\mathrm{c}}^2=1$). The spectral functions of the valence and conduction bands (equation (13)) have a similar form to that of a BCS superconductor (equation (6)). The renormalized dispersions $\Omega_{\pm}$ also represent a band structure gapped at $E_{\mathrm{F}}$ (a self-consistent calculation of the chemical potential is, however, not included in the model).

In figure 4(a), we plot the dispersions[10] in the normal phase (i.e. with $\Delta=0\,\mathrm{meV}$) for a semimetal, with a gap of $E_{\mathrm{G}}=-0.07\,\mathrm{eV}$ (overlap). Figure 4(b) presents the renormalized dispersions calculated with the roots $\Omega_{\pm}(\vec{k})$ of equation (12) in the excitonic insulator phase (with $\Delta=100\,\mathrm{meV}$). Many different features should be emphasized.

- In the excitonic insulator phase, the dispersions at $\Gamma$ are identical to those at $M$.[11] This is the manifestation of the CDW associated with this exotic phase.
- Similarly to the BCS theory, a gap opens at $E_{\mathrm{F}}$. However, as we will see in the generalized case of the next section, this particularity is not intrinsic to the theory but specific to the initial band structure. The gap always opens at the crossing of the valence and conduction bands. This causes the system to become insulating in the LT phase (provided the chemical potential stays in the gap).

[10] We will distinguish between the dispersion, where only the energy as a function of the wave vector $\vec{k}$ is considered, and the band, which is a dispersion carrying a SW.

[11] This stems from the fact that all Green's functions have the same denominator (equation (11)).

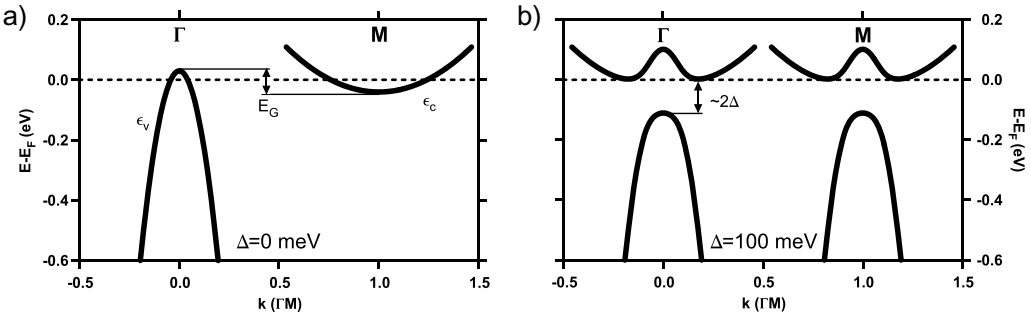


**Figure 4.** (a) Dispersions in the normal phase ($\Delta = 0$ meV) for a semimetallic configuration. (b) Renormalized dispersions in the excitonic insulator phase (for $\Delta = 100$ meV).

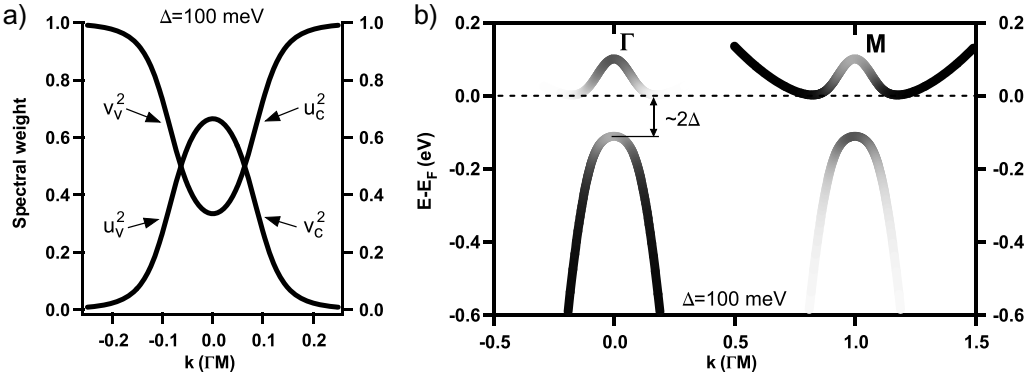


**Figure 5.** (a) SWs of the renormalized valence and conduction bands in the excitonic insulator phase (for $\Delta = 100$ meV). (b) Renormalized dispersions of figure 4(a) with their respective SWs.

- The valence band splits into two parts and its main part shifts to higher binding energies in the occupied states. The conduction band disperses now above $E_F$, displaying a non-trivial shape, since, around $M$, it deviates from its initial parabolic shape and follows now the top of the former valence band. This can be seen as hybridization between these two bands.

To get a complete picture of the spectroscopic signature of the excitonic insulator phase, we have to add the SWs to the dispersions of figure 4. It turns out that the four different coherence factors of equation (14), which are nothing else than the SWs seen in photoemission, reduce to only two different ones, since $u_v^2 = v_c^2$ and $v_v^2 = u_c^2$. They are plotted in figure 5(a), for $\Delta = 100$ meV. We see graphically that they obey the sum rules $u_v^2 + v_v^2 = 1$ and $u_c^2 + v_c^2 = 1$. Figure 5(b) shows the renormalized dispersions with their respective SWs, for $\Delta = 100$ meV. We note the following changes with respect to the previous picture in figure 4(b).

- The band structure at Γ is not identical to that at $M$ anymore. The SW distributions break this equivalence, so that the CDW appears only partially due to photoemission.
- Due to the sum rules seen above, the SW lost in the valence band at Γ is totally transferred into its backfolded version at $M$ and vice versa for the conduction band at $L$ and its backfolded version at Γ.

## 5. The exciton condensate phase (four bands)

### 5.1. Main analytical results

We now study the excitonic insulator phase model of section 2 for the four-band model electronic structure of $1T$-$TiSe_2$. It consists of the topmost valence band at $\Gamma$ and three symmetry equivalent conduction bands at $L$ (black thick lines in figures 2(b) and (c)), described by the dispersions $\epsilon_v(\vec{k})$ and $\epsilon_c^i(\vec{k})$ $(i = 1, 2, 3)$, respectively. These dispersions have been chosen to be of the form

$$\epsilon_v(\vec{k}) = \hbar^2 \frac{k_x^2 + k_y^2}{2m_v} + t_v \cos\left(\frac{2\pi k_z}{2k_{\Gamma A}}\right) + \epsilon_v^0, \tag{15}$$

$$\epsilon_c^i(\vec{k}) = \frac{\hbar^2}{2m_L}((\vec{k} - \vec{w}_i)\cdot\vec{e}_{i\parallel})^2 + \frac{\hbar^2}{2m_S}((\vec{k} - \vec{w}_i)\cdot\vec{e}_{i\perp})^2 + t_c \cos\left(\frac{2\pi(k_z - w_{iz})}{2k_{\Gamma A}}\right) + \epsilon_c^0, \tag{16}$$

which describe well the bands near their extrema as they are measured in ARPES [5]. The unit vectors $\vec{e}_{i\parallel}$ and $\vec{e}_{i\perp}$, pointing along and perpendicular to the long axis of the ellipses, respectively, form a local in-plane basis for the electron pockets at the different $L$ points. The $m_v$, $m_L$ and $m_S$ are the effective masses of the valence band holes and of the conduction band electrons along the long and short axes of the electron pockets, respectively. The hopping parameters $t_v$ and $t_c$ represent the amplitudes of the dispersions perpendicular to the surface and $k_{\Gamma A}$ is the distance in reciprocal space between $\Gamma$ and A. Parameters $\epsilon_v^0$ and $\epsilon_c^0$ are the extrema of the bands.

The Green's functions of the valence and conduction bands have already been calculated in detail in a previous work [15]. Therefore, only the final results are recalled here

$$G_v(\vec{p}, z) = \frac{1}{\mathcal{D}(\vec{p}, z)} \cdot \prod_i \left(z - \epsilon_c^i(\vec{p} + \vec{w}_i)\right), \tag{17}$$

$$G_c^i(\vec{p}, z) = \frac{1}{\mathcal{D}(\vec{p}, z)} \cdot \left((z - \epsilon_v(\vec{p})) \prod_{j\neq i} \left(z - \epsilon_c^j(\vec{p} + \vec{w}_j)\right) - \sum_{m,j\neq i} |\Delta_j(\vec{p})|^2 |\varepsilon_{ijm}| \left(z - \epsilon_c^m(\vec{p} + \vec{w}_j)\right)\right) \tag{18}$$

($\varepsilon_{ijm}$ is the permutation symbol).

The denominator $\mathcal{D}$, common to all Green's functions, is

$$\begin{aligned}\mathcal{D}(\vec{p}, z) &= (z - \epsilon_v(\vec{p})) \prod_i \left(z - \epsilon_c^i(\vec{p} + \vec{w}_i)\right) - \sum_i |\Delta_i(\vec{p})|^2 \prod_{j\neq i} \left(z - \epsilon_c^j(\vec{p} + \vec{w}_j)\right) \\ &= \prod_{\alpha=1}^{4} (z - \Omega_\alpha(\vec{p}))\end{aligned} \tag{19}$$

(here the index $\alpha$ refers to the four zeros of the denominator $\mathcal{D}$, while the other indices refer to the three conduction bands). In the last line, the denominator is factorized in terms involving its four (real) zeros $\Omega_\alpha(\vec{p})$, which are not only functions of the wave vector $\vec{p}$, but also implicitly functions of the order parameter[12]. The functions $\Omega_\alpha(\vec{p})$ are the renormalized dispersions in the exciton condensate phase.

[12] These zeros can be calculated exactly. However, their analytical forms are too long to be written here.

Here $\Delta_i(\vec{p})$ is the order parameter describing the exciton condensate phase. Similarly to its homonym in the BCS theory, it obeys a gap equation

$$\Delta_i(\vec{p}) = -\mathrm{i}\sum_{\vec{q}} V_{\mathrm{c}}(\vec{q}) F_i^{\dagger}(\vec{p}+\vec{q}, t=0) \tag{20}$$

involving an anomalous Green's function defined as $F_i(\vec{p}, t, t') = (-\mathrm{i})\langle T b_i(\vec{p}, t) a^{\dagger}(\vec{p}, t')\rangle$.

The corresponding spectral functions are also recalled here

$$\begin{aligned} A_{\mathrm{v}}(\vec{p}, \Omega) &= \sum_{\alpha=1}^{4} P_{\alpha}^{\mathrm{v}}(\vec{p})\, \delta(\Omega - \Omega_{\alpha}(\vec{p})), \\ A_{\mathrm{c}}^{i}(\vec{p}+\vec{w}_i, \Omega) &= \sum_{\alpha=1}^{4} P_{\alpha}^{\mathrm{c}_i}(\vec{p})\, \delta(\Omega - \Omega_{\alpha}(\vec{p})), \end{aligned} \tag{21}$$

where the weights $P_{\alpha}(\vec{p})$ (which are also implicitly functions of the order parameter $\Delta$) associated with the poles $\Omega_{\alpha}$ are

$$P_{\alpha}^{\mathrm{v}}(\vec{p}) = \frac{\prod_i (\Omega_{\alpha} - \epsilon_{\mathrm{c}}^{i}(\vec{p}+\vec{w}_i))}{\prod_{\beta\neq\alpha}(\Omega_{\alpha} - \Omega_{\beta})},$$

$$P_{\alpha}^{\mathrm{c}_i}(\vec{p}) = \frac{(\Omega_{\alpha} - \epsilon_{\mathrm{v}}(\vec{p}))\prod_{n\neq i}\left(\Omega_{\alpha} - \epsilon_{\mathrm{c}}^{n}(\vec{p}+\vec{w}_n)\right)}{\prod_{\beta\neq\alpha}\left(\Omega_{\alpha} - \Omega_{\beta}\right)} - \frac{\sum_{m,n\neq i} |\Delta_n(\vec{p})|^2 |\epsilon_{inm}| (\Omega_{\alpha} - \epsilon_{\mathrm{c}}^{m}(\vec{p}+\vec{w}_n))}{\prod_{\beta\neq\alpha}\left(\Omega_{\alpha} - \Omega_{\beta}\right)}.$$

Using the threefold symmetry of the system, we get rid of the index of the order parameter, setting $\Delta(\vec{k}) \equiv \Delta_i(\vec{k})$ (the possibility of a phase difference is not considered here, as the absolute modulus of $\Delta$ only appears in our final formulae). Until now, to ensure the generality of the theory, we always kept the $\vec{k}$-dependence of the order parameter $\Delta(\vec{k})$. However, in the practical analysis that will follow, we will use a $\vec{k}$-independent order parameter used as a free parameter.

In figure 6, the dispersions and their SWs, at $\Gamma$ and at $L$, calculated with the formulae of equation (21), are shown for different values of the order parameter $\Delta$ along the high symmetry directions $\Gamma M$ and $AL$, which coincide with the long axis of the electron pocket ellipsis. As in the case of the BCS theory, the order parameter $\Delta$ in equation (19) is a good indicator of the strength of the band renormalization in the exciton condensate phase. Moreover, since this denominator is the same for both the valence and conduction bands, we see that the valence band at $\Gamma$ is backfolded at $L$ and that the conduction bands at $L$ are backfolded at $\Gamma$ (as expected from the electron–hole coupling). This is a first indication of the CDW phase in the system. In graphs (a), (b) and (c) of figure 6, we show the dispersions of the valence and conduction bands for $\Delta = 0$, 20 and 100 meV, respectively. The labels $v_1$, $c_1$, $c_2$ and $c_3$ refer to the four different poles of the Green's functions, being identified as the valence band ($v_1$) and the three symmetry equivalent conduction bands ($c_1$, $c_2$, $c_3$). The band labelled $c_2$ carries in fact zero SW for every $k$ along $\Gamma M$ and $AL$ and is therefore not visible in figure 6. Besides the position of the bands, the spectral function contains an additional piece of crucial information, namely the SW carried by each band in the process of one-electron removal probed by photoemission. It is related to the numerator of the spectral function. This feature is depicted in grayscale in figure 6. The evolution from the normal phase (figure 6(a)) to the CDW phase with an order parameter of 20 meV (figure 6(b)) and 100 meV (figure 6(c)) is shown.

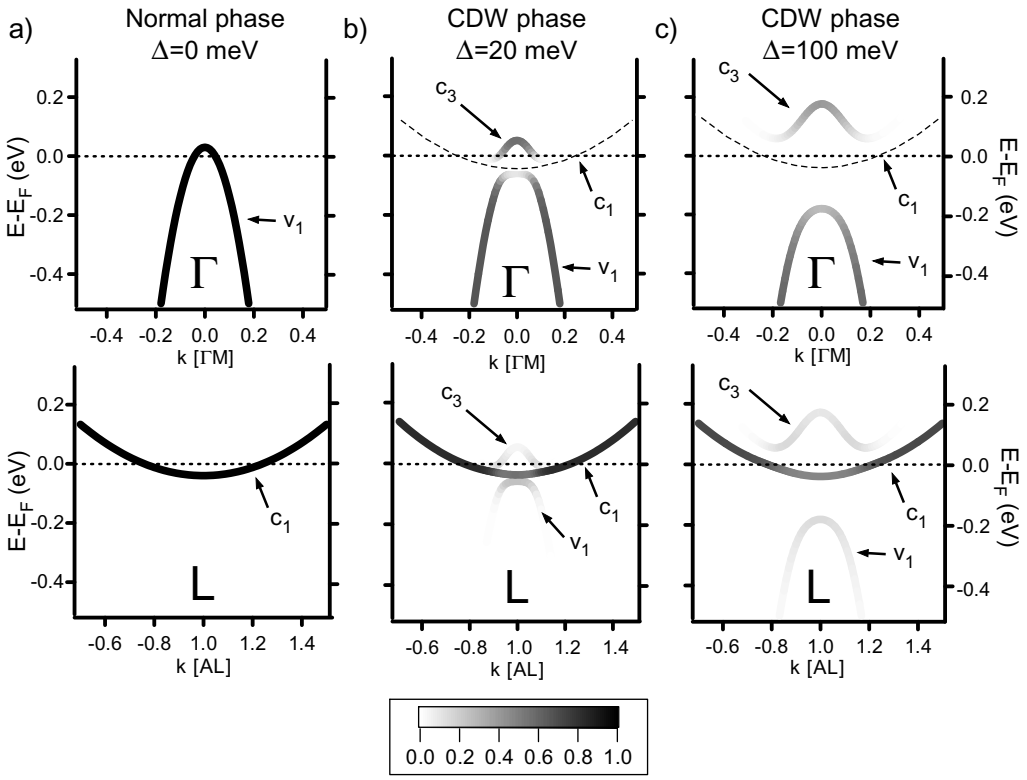


**Figure 6.** Band dispersions with their corresponding SW at Γ and $L$, along the $\Gamma M$ and $AL$ directions, respectively: (a) the normal phase ($\Delta = 0$ meV), (b) the CDW phase with moderate excitonic effects ($\Delta = 20$ meV) and (c) the CDW phase with strong excitonic effects ($\Delta = 100$ meV). The dashed lines indicate a band ($c_1$) having a small non-zero SW.

In the normal phase, the band structure consists here of a valence band at Γ having its maximum at +30 meV and three symmetry equivalent conduction bands at $L$ having their minima at −40 meV. The effective mass of the conduction band being larger than that of the valence band, this configuration describes an uncompensated semimetal, meaning that the number of electrons is larger than that of holes. This configuration has been obtained from fits to the spectra measured on $1T$-$TiSe_2$ [15]. Such an electron doping can be explained in these samples by an uncontrolled excess of Ti atoms occurring during crystal growth [22] and corresponds to about 1% of excess Ti. A more detailed analysis of this topic can be found in [15].

In figure 6, we immediately see that, with respect to the SW, the backfolding is in fact incomplete even at a large value of the order parameter. In the CDW phase with an order parameter of $\Delta = 100$ meV (figure 6(c)), at Γ, the original valence band loses SW in favor of the backfolded conduction band ($c_3$). The dashed lines indicate a conduction band ($c_1$) backfolded to Γ, which has a negligibly small SW (see below). At $L$, the situation is different. Two backfolded bands appear now, namely a symmetry equivalent conduction band ($c_3$) and the valence band ($v_1$), taking their SW from the original conduction band ($c_1$). A major difference compared to the two-band excitonic insulator of section 4 is that, whatever the value of the order parameter, there is always a band remaining here at its original position (when not considering any change

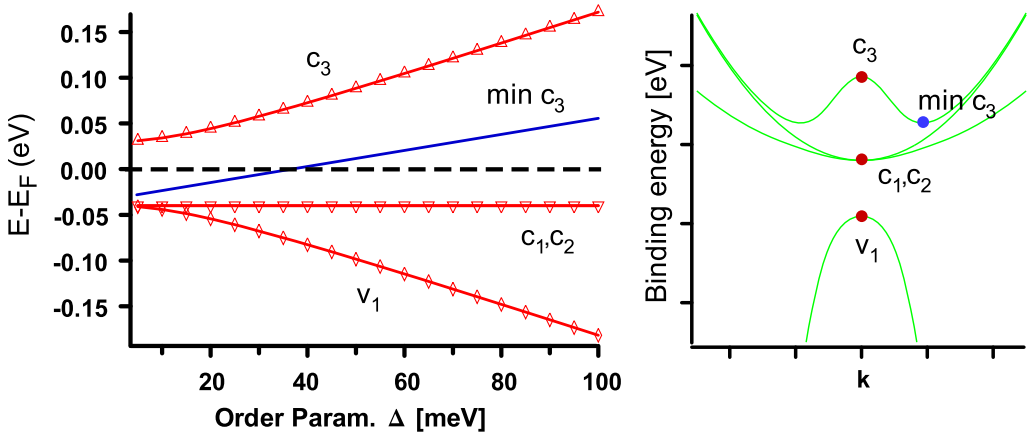


**Figure 7.** Extrema of the renormalized dispersions as a function of the order parameter $\Delta$ (left). Positions of these extrema on the dispersions (right).

in the chemical potential), which is in this case at the Fermi energy at $L$ (the original conduction band $c_1$), so that the system is never really insulating. The larger the order parameter, the larger the transfer of SW from this band to the others, but it always keeps a non-negligible SW. For this reason, strictly speaking, the denomination *excitonic insulator phase* in this context is misleading and we rather adopted the expression *exciton condensate phase*. This matter of fact depends, of course, on the position of the conduction band $c_1$ in the normal phase.

We now turn to the discussion of the extrema of the bands. Figure 7 presents the band extrema as a function of the order parameter $\Delta$. We see that, except for small values of the order parameter, they display linear behavior (this can be shown analytically from the denominator in equation (19) for $\vec{k}$ exactly at $\Gamma$ or $L$ where the three original conduction bands have the same energy). Among the three conduction bands, only one ($c_3$) shifts away from the Fermi energy and the other bands ($c_1$, $c_2$) remain at their original position. Its two minima (blue line) also increase linearly. Compared to the conduction band $c_3$, the valence band maximum ($v_1$) follows the inverse behavior, thereby opening a gap below $E_F$. The distance between $v_1$ and $c_3$ is approximately $|E_G| + 2\Delta$.

### *5.2. Comparison with the experiment*

In this section, we summarize ARPES results on $1T$-$TiSe_2$ and compare them to photoemission intensity maps calculated within our exciton condensate phase model [5, 15]. At the photon energy of 31 eV, the normal emission spectra correspond to states located close to the $\Gamma$ point and the surface notation $\bar{\Gamma}$ will be used for the measured intensity maps.

Figure 8 presents comparisons between the theoretical (left) and experimental (right) electronic structures at $\Gamma$ and $\bar{\Gamma}$ respectively. The experimental intensity maps at $T = 250$ K (figure 8(a)) and $T = 65$ K (figure 8(b)) are compared to calculated bands with $\Delta = 25$ meV and $\Delta = 75$ meV, respectively. These values for the order parameter in the RT and LT phases, respectively, have been chosen to ensure the best visual agreement between calculated and measured intensity maps. This gives thus an estimation of the size of the order parameter describing the exciton condensate phase in $TiSe_2$. A quantitative study of the value of the order parameter will be given in the next section (section 6.2). At $T = 250$ K on the experimental

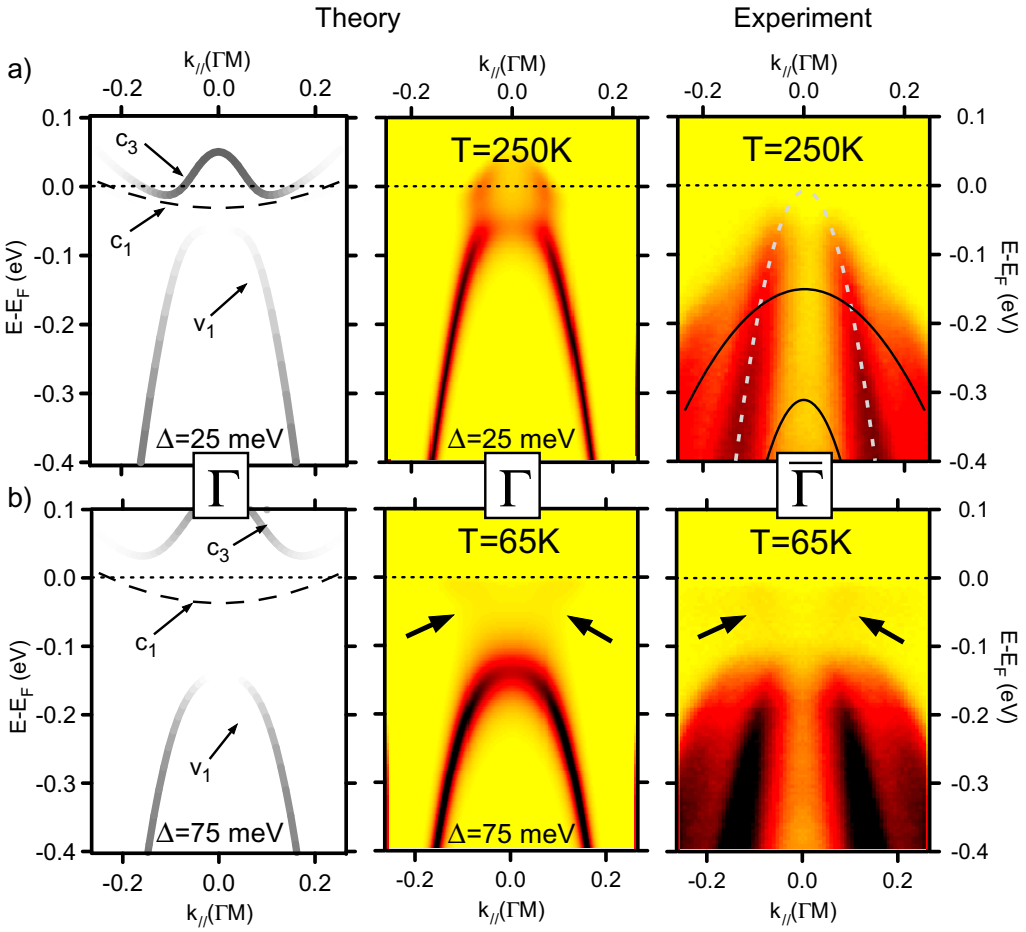


**Figure 8.** Comparisons between theoretical and experimental ($h\nu = 31$ eV) electronic structures at $\Gamma$ and $\bar{\Gamma}$, respectively (see text for an explanation of this notation). (a) The theoretical bands have been calculated for $\Delta = 25$ meV and the experimental intensity maps are taken at $T = 250$ K. The continuous black lines (plotted on the experimental data) highlight the Se4p-derived bands not considered in the model, while the dashed white line indicates the valence band corresponding to $v_1$. (b) The theoretical bands have been calculated for $\Delta = 75$ meV and the experimental intensity maps are taken at $T = 65$ K. The dashed black lines indicate the backfolded conduction band $c_1$, which carries a small non-zero SW. The calculated photoemission intensity maps in the middle panel have been obtained by broadening the delta peaks of the left panel with a constant imaginary part of 30 meV. Black arrows indicate the remaining SW.

side (figure 8, right), the situation is more complicated than in our model. Indeed, there are three Se4p-derived valence bands, out of which two (black lines) are not considered in our model (see also figure 2(b), right). The dashed white line corresponds to the valence band $v_1$ of the model, which suffers already SW loss at $T = 250$ K. It flattens at its maximum and deviates from the parabolic shape of the normal phase dispersion (this is clear from energy distribution curves (EDCs) taken close to $k_\parallel = 0$ Å$^{-1}$, not shown here). On the theoretical side

(figure 8(a), left), the $\delta$-peak-like dispersion reproduces well the experiment when considering an order parameter of $\Delta = 25$ meV. A calculated photoemission intensity map is also shown at the center. A constant 30 meV imaginary part has been added to the denominator of the Green's functions to widen the $\delta$-peaks. However, at this temperature, the system should be in the normal phase and the order parameter should be zero. Nevertheless, as in high temperature superconductors, above the critical temperature, we expect fluctuations to persist well above $T_c$ in the exciton condensate phase [33, 34]. Thus, this non-zero order parameter above $T_c$ is used to model such fluctuations, anticipating the condensate phase. This approach will be confirmed quantitatively in section 6. The most striking consequence of this non-zero order parameter is to shift the valence band $v_1$ into the occupied states, leaving a small part of it at $E_F$ and opening a kind of pseudo-gap just below $E_F$. Furthermore, according to the theory graphs of figure 8(a) (on the left), the bottom of the backfolded conduction band $c_3$ appears just below $E_F$. This is even more clear in the calculated maps (center), where some residual intensity appears at $E_F$. In parallel, the experiment shows small maxima in momentum distribution curves near $E_F$ (not seen in the false color map with limited dynamic range). These can be attributed to $c_3$.

At $T = 65$ K (figure 8(b), right), the valence band in the experimental intensity map shifts to higher binding energies, in agreement with the theoretical dispersions calculated for an order parameter $\Delta = 75$ meV (figure 8(b), left). Moreover, on the experimental map, some intensity emerges just below $E_F$, as one can see on the map with saturated color scale, revealing a dispersive feature. While it does not appear directly in the corresponding calculation using $\delta$-peaks, it is reproduced on the broadened calculated photoemission intensity map in the center. In other words, this dispersive intensity comes from the combined tails of the maximum of the valence band $v_1$ (located in the occupied states) and of the minima of the backfolded conduction band $c_3$ (located in the unoccupied states).

Figure 9 presents comparisons between the theoretical and experimental electronic structures at the BZ boundary. The experimental intensity maps at $T = 250$ K (figure 9(a)) and $T = 65$ K (figure 9(b)) are compared to calculated bands with $\Delta = 25$ meV and $\Delta = 75$ meV, respectively. At a photon energy of 31 eV, initial states between $M$ and $L$ are probed (in a free electron final state picture, we are not probing the BZ exactly at $L$) and the $\bar{M}$ notation is used for the measured intensity maps. At $T = 250$ K (figure 9(a)), on the experimental side (right), the conduction band, highlighted by the dashed white line, is well described by the theoretical band $c_1$ (left). It also exhibits a decrease of intensity at its bottom and it looks like a band having a large width with surprisingly high intensity even at binding energies of about 300 meV. These features can be explained by the theoretical bands (figure 9, left) at $\Delta = 25$ meV, where fluctuations in the high-temperature phase are modeled by this non-zero order parameter. Adding a finite width to the $\delta$-peak-like bands, one sees (central graph in (a)) that the conduction band $c_1$ merges with its close (backfolded) neighbors $v_1$ or $c_3$ (depending on the position along $AL$), resulting in a band broadening. The residual intensity at high binding energies is explained with the populated branches of the backfolded valence band $v_1$.

At $T = 65$ K (figure 9(b)), on the experimental side (right), a strong signature of the CDW appears. The valence band is backfolded at $\bar{M}$ with a high SW. In fact, even a second Se4p-derived valence band (indicated by the lowest lying black line in the right graph of figure 8(a)) participates in the backfolding at $\bar{M}$. On the theoretical side, this situation (considering only the topmost Se4p-derived valence band) is reproduced with an order parameter of $\Delta = 75$ meV. The backfolded valence band $v_1$ is well separated from the conduction band $c_1$, as in the experiment. It can be clearly seen in the corresponding

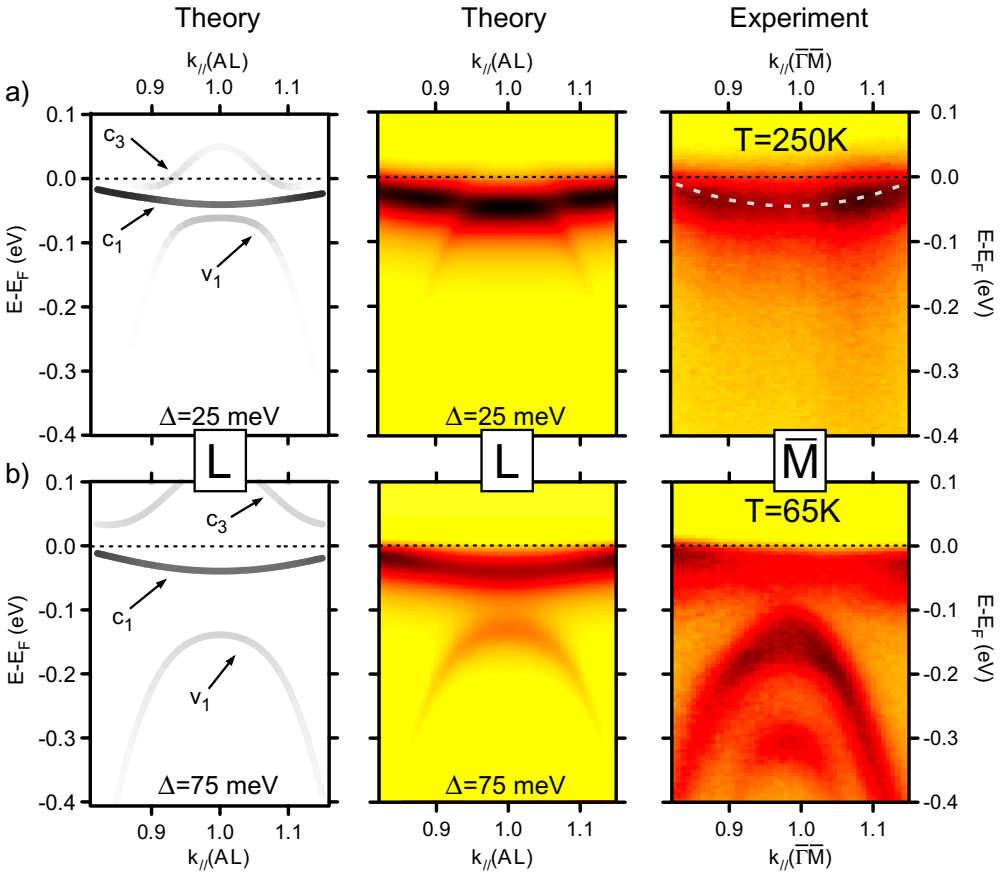


**Figure 9.** Comparisons between theoretical and experimental ($h\nu = 31$ eV) electronic structures at the BZ boundary (see text). (a) The theoretical bands have been calculated for $\Delta = 25$ meV and the experimental intensity maps are taken at $T = 250$ K. The dashed white line indicates the conduction band corresponding to $c_1$. (b) The theoretical bands have been calculated for $\Delta = 75$ meV and the experimental intensity maps are taken at $T = 65$ K. The calculated photoemission intensity maps in the middle panel have been obtained by broadening the delta peaks of the left panel with a constant imaginary part of 30 meV.

experimental intensity map that the conduction band $c_1$ does not shift with increasing order parameter (see figure 7) and loses more SW at its bottom. In the model, at $L$, the intensity of the backfolded valence band $v_1$ is lower than that of the conduction band $c_1$ for high values of the order parameter, corresponding to a well-established CDW phase. In the ARPES measurements presented here, this intensity relation is reversed, as can be seen in the right graph of figure 9(b). The precise reason for this remains unclear. We recall here that only electronic degrees of freedom are considered in our model. However, the PLD, developing in $1T$-$TiSe_2$ and concomitant to the CDW [22], should be included in the model and its influence calculated self-consistently with the exciton condensate phase. Such a calculation is challenging and has not yet been performed. Nonetheless, one can suppose that the PLD enhances the effect of the exciton condensate.

### *5.3. Conclusions from the comparison*

The good agreement between the photoemission intensity maps calculated within the exciton condensate phase model and the experimental data leads us to give strong support for the realization of this exotic phase in $1T$-$TiSe_2$. However, a band Jahn–Teller scenario may produce the same spectral function and thus the same calculated photoemission intensity maps. As we have seen in section 5.1, the SW of the backfolded bands in the CDW phase is closely related to the order parameter, whose amplitude is notably given by the Coulomb interaction between the electrons and holes in the case of the exciton condensate phase. In the case of the band Jahn–Teller effect, the formalism would be the same, but the interaction responsible for CDW phase is then the electron–phonon interaction [27, 35]. Nevertheless, the fact that the backfolded valence band at $L$ exhibits a high intensity, despite the relatively small atomic displacements ($\sim$0.08 Å) observed for $1T$-$TiSe_2$ [22], gives less credibility to the band Jahn–Teller effect. Indeed, it is well known that the intensity in the backfolded bands is proportional to the strength of the new potential of competing periodicity in the case of a CDW phase [36, 37]. In other words, from the small atomic displacements in the CDW phase, we do not expect the electron–phonon interaction at $L$ to play a leading role in the occurrence of the strong backfolded valence bands.

## 6. Temperature dependence

In this section, we study the temperature dependence of the features evidenced previously with the help of the exciton condensate phase model.

### *6.1. Temperature dependence in the model*

First, we focus on the model and study how its spectroscopic features evolve with temperature.

In the previous section, visual agreement between measured and calculated photoemission intensity maps allowed us to roughly estimate the order parameter in the condensate phase. However, a more systematic and more precise determination of this order parameter as a function of temperature, based on photoemission measurements, represents a very profitable improvement. For that purpose, and to anticipate the experimental work of section 6.2, we perform a theoretical analysis of the model and introduce temperature effects in a simple way, by choosing a particular form for the order parameter, namely $\Delta(T) = \Delta_0 \cdot \sqrt{1-(T/T_c)^2}$ where $\Delta_0$ is its value at $T = 0$ K. This function is drawn in figure 10(a) for $\Delta_0 = 100$ meV and $T_c = 200$ K. In that sense, we are modeling the temperature dependence in order to see what can be expected from photoemission measurements. We first fix a particular temperature dependence, insert it in the model (in the denominator of equation (19) to calculate the renormalized dispersions as a function of temperature, and then in equations (21) to obtain the SWs) and then visualize the evolution of the spectra with temperature.

The renormalized dispersions at $\Gamma$ and $L$ as a function of temperature are displayed in figure 10(b). Below the transition temperature, the backfolded valence band $v_1$ and conduction band $c_3$ shift away from their normal phase positions, exhibiting behavior very similar to the shape of the order parameter. At the same time, the conduction band $c_1$ and a symmetry equivalent version $c_2$ stay at their initial positions. Considering also SWs and broadening the $\delta$-like peaks with a finite width of 30 meV (for presentation purposes), figure 10(c) displays over

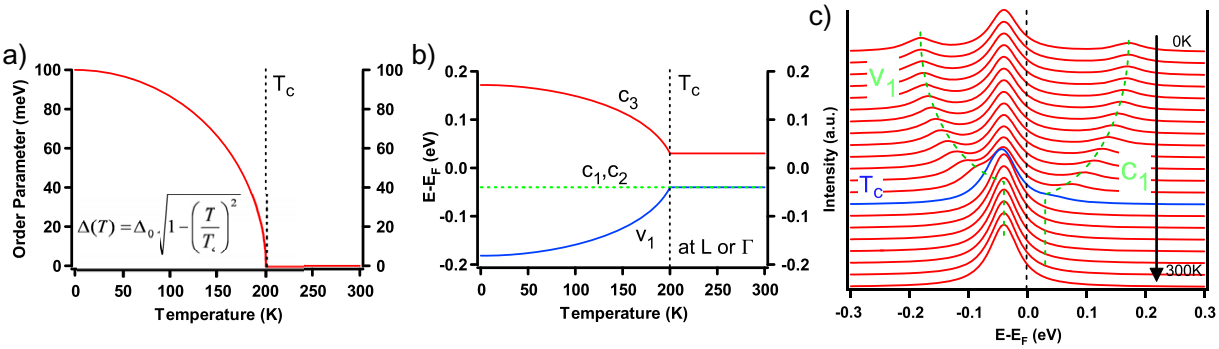


**Figure 10.** (a) BCS-like temperature dependence chosen for the order parameter. (b) Position of the bands at Γ and $L$ as a function of temperature for the order parameter in graph (a). (c) Evolution of the broadened spectra (see text) at $L$ under the effect of temperature.

a wide temperature range spectra at $L$ (not equivalent to Γ due to the SWs). This region of the BZ has been chosen, because there the excitonic effects are the most spectacular and occur in the occupied states, accessible to ARPES. Below $E_F$, one sees that the evolution of the backfolded valence band $v_1$ is characteristic of the temperature dependence of the order parameter. These calculated spectra highlight how the real temperature behavior of the order parameter can be extracted experimentally from ARPES data. Precisely these features will be exploited in the next section to obtain $\Delta(T)$ experimentally.

Having the spectral function for the exciton condensate phase as a function of temperature, we can also compute the temperature dependence of the chemical potential $\mu$, using the condition of conservation of occupied electronic states (weighted with the SWs $P_\alpha$), whose densities around Γ and $L$ are computed with

$$n = n_\Gamma + n_L = \sum_{\alpha=1}^{4} \int \frac{d\vec{k}}{4\pi^3} P_\alpha^v(\vec{k}) N_F(\Omega_\alpha(\vec{k}) - \mu) + \frac{3}{2} \sum_{\alpha=1}^{4} \int \frac{d\vec{k}}{4\pi^3} P_\alpha^c(\vec{k}) N_F(\Omega_\alpha(\vec{k}) - \mu). \quad (22)$$

The factor of $\frac{3}{2}$ occurs, because there are three halves of an ellipse in the BZ. First we study the evolution of the chemical potential for our four-band system in the normal phase, fixing $\Delta_0 = 0$ meV (with no CDW phase). In such a system, any change in the chemical potential as a function of temperature is related to the population of the valence and conduction bands due to the Fermi–Dirac distribution and is thus sensitive to the ratio of the effective masses. Then we fix $\Delta_0 = 100$ meV for the excitonic insulator system. Figure 11(a) shows the behavior of the chemical potential for these two cases. One sees that without excitonic effects, a system having the modelized configuration of $TiSe_2$ undergoes already a chemical potential shift of about 12 meV over the range of 300 K due to the change in the thermal occupation of electronic states and the different effective masses. If an excitonic phase transition with $\Delta_0 = 100$ meV sets in, a drastic change happens at $T_c$ and the chemical potential shift increases up to nearly 60 meV. This large additional shift of the chemical potential is necessary to compensate for the occupied electronic states lost below $T_c$ at Γ in the valence band $v_1$ and at $L$ in the original conduction band $c_1$ (the states gained in the backfolded valence band at $L$ are not sufficient to compensate for this loss). Such a large shift should be visible in ARPES, but it must be emphasized that this holds only for the simplified $1T$-$TiSe_2$ electronic bandstructure of this model (in particular without considering the other Se4p-derived valence bands and the conduction bands at $L'$).

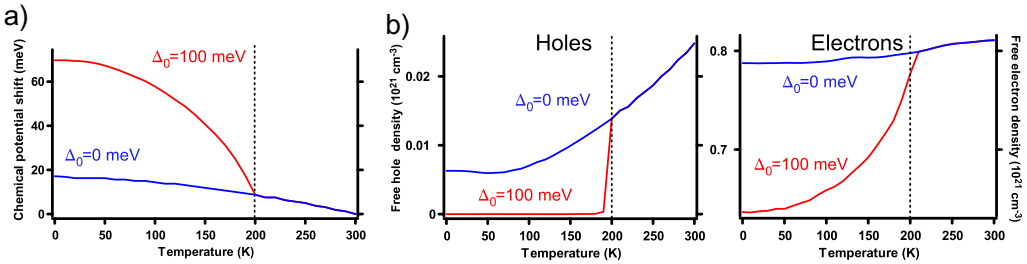


**Figure 11.** Compared behavior for the cases of a simple semi-metallic system (i.e. $\Delta_0 = 0$ meV, in blue) and an excitonic insulator (i.e. $\Delta_0 = 100$ meV, in red). (a) Temperature dependence of the chemical potential. (b) Temperature dependence of the free hole (left) and electron (right) density.

Knowing the band dispersions around $E_F$ and their shift due to the combined effect of the chemical potential and the order parameter, it is also possible to compute the free carrier density $n = n_{\text{hole}} + n_{\text{electron}}$ in the system, composed of holes in the valence band and electrons in the conduction bands. These quantities will provide us with a key component for understanding the anomalous resistivity of $1T$-$TiSe_2$. For that purpose, we use again formulae like that of equation (22), collecting the electrons in the conduction bands and the holes in the valence band. Figure 11(b) (left) shows the free hole density as a function of temperature. In comparison with the normal metal ($\Delta_0 = 0$ meV), in the exciton condensate phase ($\Delta_0 = 100$ meV), the free hole density is strongly suppressed below $T_c$. This can be explained with figures 6(a), (b) and (c). As the order parameter increases from a zero value, a gap opens at $\Gamma$, shifting the valence band $v_1$ into the occupied states, depriving the system of a primary source of holes.

As explained in section 5, the four-band electronic structure considered here is that of an uncompensated semimetal, with about 1% of excess Ti, doping the system with negative charge carriers. Therefore the free electron density is higher than the free hole density. The chemical potential $\mu$ is pinned in the bottom of the conduction bands due to the excess electron doping. In figure 11(b) (right), the free electron density of the excitonic insulator displays also a strong decrease below $T_c$. Indeed, at $L$, the bottom of the conduction band $c_1$ loses SW, reducing the free electron carrier density. In parallel, the chemical potential moves upward in the conduction band (this shift is nonetheless smaller than the gap produced by the order parameter), making available new states in the conduction band $c_1$ with higher SW than those at its bottom. However, this is not sufficient to counterbalance the previous effect.

In transport measurements, the CDW has a strong signature, raising the resistivity $\rho$ below $T_c$ as in a (weak) insulator. Having now an approximate behavior of the free charge carrier density as a function of temperature, we can also estimate the resistivity in the Drude theory by $\rho = m/ne^2\tau$, with $\tau$ being the relaxation time and $m$ the effective mass. This will be the main purpose of section 7, based on experimental observations.

### *6.2. Temperature dependence from the experiment*

In the previous section, we have calculated the spectroscopic signature of the temperature dependence of the order parameter in the photoemission spectra, allowing us to realize that the behavior of the backfolded valence band at $L$ is characteristic of that of this order parameter. We also pointed out a chemical potential shift developing especially in the CDW phase due to the

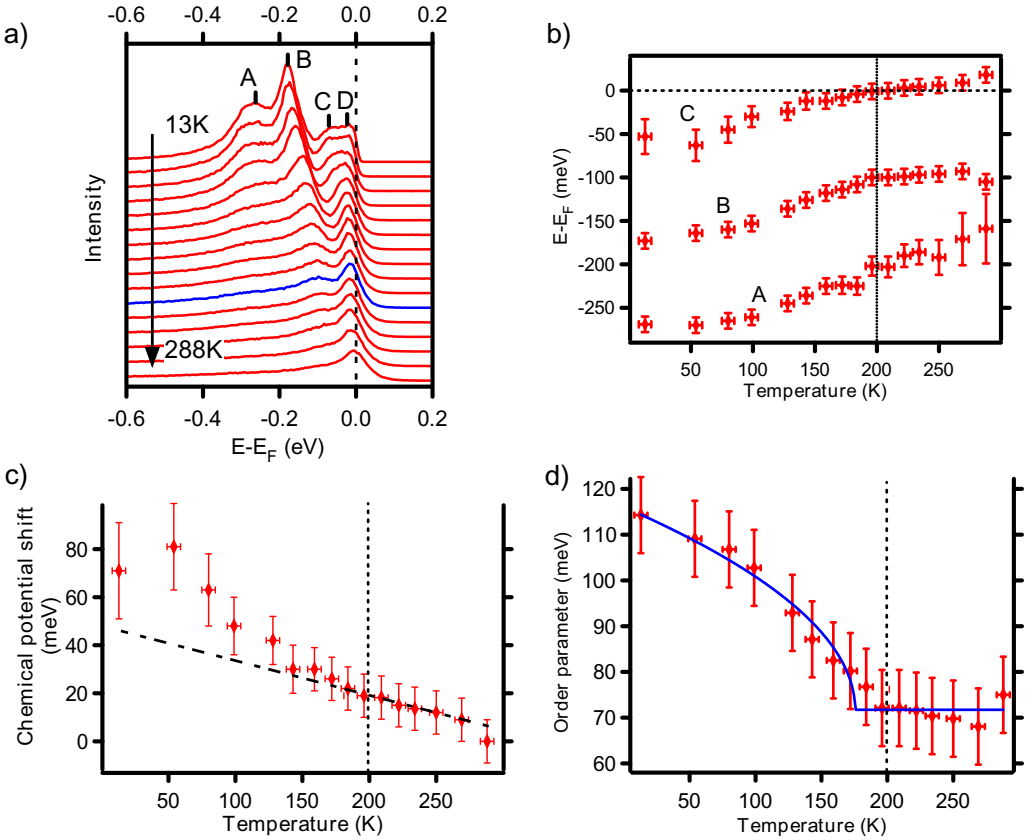


**Figure 12.** (a) EDCs measured exactly at $\bar{M}$, as a function of temperature (for the blue EDC, $T = 200$ K). (b) Position of contributions A, B, and C as a function of temperature, obtained by fitting EDCs, and with their error bars. (c) Chemical potential shift obtained from our data. The dotted–dashed line represents the extrapolation of a linear fit to the high temperature part. (d) Order parameter of the exciton condensate phase. The continuous (blue) line is a fit to a mean-field-like function.

SW transfers. Therefore, in this section, we present photoemission intensity maps measured at $\bar{M}$ (but close to $L$) over a wide temperature range with small steps to evaluate these quantities. For each measurement, we extract the EDC exactly at $k_{\|} = |AL|$, where the valence and conduction bands reach their extrema.

The waterfall of figure 12(a) collects such EDCs as a function of temperature. The blue EDC was measured at 200 K (at $T_c$). The conduction band, labeled $C$, is clearly recognized just below $E_F$. At LT, a new peak, labeled $B$, develops below the conduction band and is identified as the valence band backfolded to $\bar{M}$. With decreasing the temperature, it shifts to higher binding energies and becomes much more intense. Another peak, labeled $A$, also develops below this backfolded band, which can be identified with a second (spin–orbit split) valence band backfolded from $\bar{\Gamma}$ to $\bar{M}$. Looking carefully at the situation near $E_F$ at the lower temperatures, one distinguishes a fourth contribution $D$, barely resolved here, which disappears at higher temperatures. We identify this peak as the quasi-particle peak originating from the coupling of the conduction band to phonons as elaborated for surface states in the study of

Hengsberger *et al* [38]. Contribution $C$ is then the incoherent peak that mostly follows the dispersion of the original conduction band.

To obtain more information from the data of figure 12(a), we have fitted the EDCs. Figure 12(b) shows the position of contributions $A$, $B$ and $C$ as a function of the temperature, which are the two backfolded valence bands and the conduction band, respectively. All three bands undergo a shift towards $E_F$ as the temperature increases, with the largest change below $T_c$. At RT, the conduction band at $\bar{M}$ (close to $L$) lies in the unoccupied states, at 18 meV above $E_F$. This result is in apparent contradiction with the photoemission data presented in figure 9 (but in agreement with earlier ARPES studies [7, 8, 39]), where the position of the conduction band has been measured below $E_F$, at $E_{c_1} = -40 \pm 5$ meV. The answer to this problem is given by the uncontrolled Ti excess of the $1T$-$TiSe_2$ samples: the samples studied in section 5.2 contained a higher density of such excess Ti atoms, whose electrons mainly filled and shifted the conduction band into the occupied states.

As we have seen in figure 7, the order parameter $\Delta$ does not influence the minimum position of the conduction band exactly at $L$, provided the chemical potential is fixed. Therefore, in the exciton condensate phase model, any shift of this band with temperature at $L$ will signify a chemical potential shift. Figure 12(c) shows the chemical potential shift obtained with the shift of the position of the conduction band (peak C in figure 12(b)) with respect to its RT value, as a function of temperature. This curve can be compared with the one determined numerically in the previous section and shown in figure 11(a). As in this calculation, two regimes can be distinguished. Above $T_c$, a quasi-linear shift develops due to the effect of temperature on a two-band system with different effective masses (in practice, there are four bands, but the three conduction bands are symmetry equivalent). The dashed–dotted line in figure 12(c) underlines this behavior. Then, below $T_c$, a clear increase occurs due to the exciton condensation. Despite the simplicity of the electronic structure considered in our model, good agreement between the calculation and the experiment is obtained, not only qualitatively but also quantitatively.

In section 5.1, it has been stated that the roots of the denominator of the Green's function (equation (19)) represent the renormalized dispersions in the exciton condensate phase model. No general analytical form was given, since the formulae are too complicated. However, exactly at $L$, the situation simplifies drastically and the formulae become

$$\begin{aligned} \Omega_{v_1}(\Delta) &= E_{c_1} - \frac{E_G}{2} - \frac{1}{2}\sqrt{E_G^2 + 12\Delta^2}, \\ \Omega_{c_1}(\Delta) &= E_{c_1}, \quad \Omega_{c_2}(\Delta) = E_{c_1}, \\ \Omega_{c_3}(\Delta) &= E_{c_1} - \frac{E_G}{2} + \frac{1}{2}\sqrt{E_G^2 + 12\Delta^2}, \end{aligned} \tag{23}$$

with $E_{c_1} = 18$ meV, the position of the conduction band at RT, and $E_G := E_{c_1} - E_{v_1} = -12$ meV, the gap between the valence and conduction bands in the normal phase, which in our case is an overlap ($E_{v_1} = 30$ meV is the position of the valence band for $\Delta = 0$ meV taken from the study of section 5.2) (see also [5]). These relationships are of great interest since they provide a simple way to extract the temperature dependence of the order parameter $\Delta(T)$ from the position of the backfolded bands.

In our case, as mentioned above, only the backfolded valence band $E_{v_1}(\Delta)$ is useful, since the band $c_3$ cannot be observed by photoemission. It must also be emphasized that calculations leading to relations (23) have been done in a mean-field approximation, meaning that these

relation is valid only below $T_c$. Nonetheless, we use them above $T_c$ to get an idea of the strength of fluctuations already identified in figure 9(a) (right panel) at 250 K, where there is diffuse intensity below the conduction band, which, interpreted as a precursor of the backfolded valence band, confirms this hypothesis.

Inverting thus the first equation in (23) and inserting the temperature-dependent position of the valence band of figure 12(b) ($E_{v_1}(\Delta)$, contribution $B$, which corresponds to $v_1$) results in the data points of figure 12(d). For comparison, they are superimposed on a mean-field-like order parameter of the form

$$\Delta(T) = \Delta_0 \sqrt{1 - \left(\frac{T}{\tilde{T}_c}\right)^{\alpha}} + \Delta_{\text{off}} \tag{24}$$

fitted to the experiment (continuous blue line), with $\alpha = 1$. One sees immediately that the critical temperature extracted from the ARPES data $\tilde{T}_c \simeq 175$ K is smaller than that determined from resistivity measurements [22], $T_c = 200$ K. However, the presence of electron–hole fluctuations smooths the sharpness of the mean-field-like transition, as one can guess from the curve of figure 12(d), so that it is difficult to obtain $T_c$ with the function of equation (24). To ensure the best agreement with the data, an offset value for the order parameter $\Delta_{\text{off}} = 72$ meV has to be added above $T_c$, to model roughly the strong electron–hole fluctuations above $T_c$. Once the temperature decreases below $T_c$, the order parameter displays a clear increase in a mean-field fashion. This is a strong indication of the macroscopic condensation of coherent excitons. At the lowest temperature, the order parameter reaches the value of $\Delta(T = 0\,\text{K}) \cong 120$ meV (extrapolated from $\Delta(T = 13\,\text{K}) = 116$ meV). This value allows us to estimate the strength of the coupling with the well-known BCS relationship $2\Delta(T = 0\,\text{K})/k_B T_c = 12.5$–$15.5$. This value is four times that of conventional superconductive BCS systems, suggesting that a strong coupling is at play in $1T$-$TiSe_2$ to build excitons. This is not surprising, since the pairing interaction is a weakly screened Coulomb interaction for excitons (rather than an overscreened one for Cooper pairs).

In our present understanding of the phase transition of $1T$-$TiSe_2$ within the exciton condensate phase model and based on the photoemission analysis, we believe that these strong electron–hole fluctuations above $T_c$ (enhanced by the FS topology) drive an electronic instability in the system at $T_c$, leaving an intense signature in the spectral function and producing the soft phonon mode observed by Holt *et al* [24]. Below $T_c$, the system recovers from the electronic instability by building the exciton condensate, whose influence on the electronic system is evidenced by photoemission and which naturally induces a new periodicity of the electronic density, the CDW. As a consequence of the coupling between the electrons and the lattice, (small) atomic displacements are provoked below $T_c$ in response to the new periodic potential produced by the exciton condensate. This approach is similar to what Fehske and co-workers discussed in detail by looking at the divergence of the electron–hole $T$-matrix within an effective mass model [18] and at the poles of the exciton Green's function within the EFKM [19] to build the phase diagram of the excitonic insulator phase.

## 7. Effects of the exciton condensation on the transport properties

The goal of this section is to give a better understanding of the transport properties of $1T$-$TiSe_2$, based on the knowledge presented in the previous sections. For that purpose, we first recall the

different effects at play in $1T$-$TiSe_2$, evidenced in this work with photoemission, and then relate them to transport properties.

- In the exciton condensate phase, a gap opens below the conduction band and shifts the valence band into the occupied states, as a function of $\Delta(T)$, whose behavior has been shown in section 6.2.
- As $\Delta(T)$ increases, more and more SW is transferred from the original conduction band ($c_1$) (which remains close to $E_F$) to the backfolded bands, removing charge carriers.
- The chemical potential, which has been determined in section 6.2, progressively shifts the bands into the occupied states.
- Finally, a dramatic renormalization of the effective mass of the conduction band occurs at LT [40] as shown below.

At temperatures below 100 K, a dramatic renormalization of the effective mass of the conduction band occurs. With the exciton condensate phase model, this phenomenon is reproduced qualitatively and its origin is therefore related to strong electronic correlations. However, it must be emphasized that, as the temperature drops below 100 K, the effective mass of the conduction band near its minimum *decreases* drastically, meaning that correlations in the system cause an effective mass reduction, in opposition to the common belief that strong correlations enhance the effective mass.

At these temperatures, the dispersion of the conduction band deviates largely from an ellipsoid and two parts can then be distinguished (see figure 13). Around $L$ (center of figure 13 (a)), it disperses like a paraboloid (see figure 13(b), bottom pannel), with effective masses $\tilde{m}_{L,\mathrm{light}}$ along AL (long axis of the ellipsis) and $\tilde{m}_S$ along LH (short axis). This part is called the 'light' part (labeled A in figure 13(a)). Away from $L$ (but still in the occupied states, labeled B), the effective mass along AL, $\tilde{m}_{L,\mathrm{heavy}}$, is considerably larger below 100 K and gives rise to the 'heavy' part. These effective masses have been estimated for different temperatures and are summarized in table 1.

The electrical conductivity in the relaxation time approximation for a band of dispersion $\varepsilon(\vec{k})$ in the vicinity of $E_F$ (metallic system) is given by (at zero temperature)

$$\begin{aligned}\sigma &= e^2\tau(E_F)\int_{\mathrm{occ}}\frac{\mathrm{d}^3k}{4\pi^3}M^{-1}(\vec{k})\\ &= e^2\tau(E_F)\int_{\mathrm{occ,light}}\frac{\mathrm{d}^3k}{4\pi^3}M^{-1}_{\mathrm{light}}(\vec{k}) + e^2\tau(E_F)\int_{\mathrm{occ,heavy}}\frac{\mathrm{d}^3k}{4\pi^3}M^{-1}_{\mathrm{heavy}}(\vec{k})\\ &= \sigma_{\mathrm{light}} + \sigma_{\mathrm{heavy}}\end{aligned}$$

where the integration runs over the occupied states [41]. $M(\vec{k})$ is the effective mass tensor and can be separated into the 'light' and 'heavy' parts in our case, leading to the conductivities of the 'light' and 'heavy' charge carriers, respectively. This observation leads us to consider separately these two types of charge carriers in our approach to the transport properties of $1T$-$TiSe_2$.

### *7.1. Resistivity obtained by photoemission*

We now want to use the information collected for the electron pocket at $L$ to estimate the resistivity. The easiest way to compute resistivity is to use the Drude formula

$$\rho = \frac{m}{ne^2\tau}. \tag{25}$$

**Table 1.** Renormalized effective masses of the conduction band (in units of the bare electron mass) along the long axis (AL) for the light part $\tilde{m}_{L,\mathrm{light}}$ and the heavy part $\tilde{m}_{L,\mathrm{heavy}}$, and along the short axis $\tilde{m}_S$ (LH) of its elliptic Fermi surface, as a function of temperature.

| | 13 K | 81 K | 141 K | 288 K |
|---|---|---|---|---|
| $\tilde{m}_{L,\mathrm{heavy}}$ | 50 | 15 | 6.6(7) | 6.2(7) |
| $\tilde{m}_{L,\mathrm{light}}$ | 0.4(2) | 0.5(2) | 6.6(7) | 6.2(7) |
| $\tilde{m}_S$ | 0.5(2) | 0.8(2) | | |

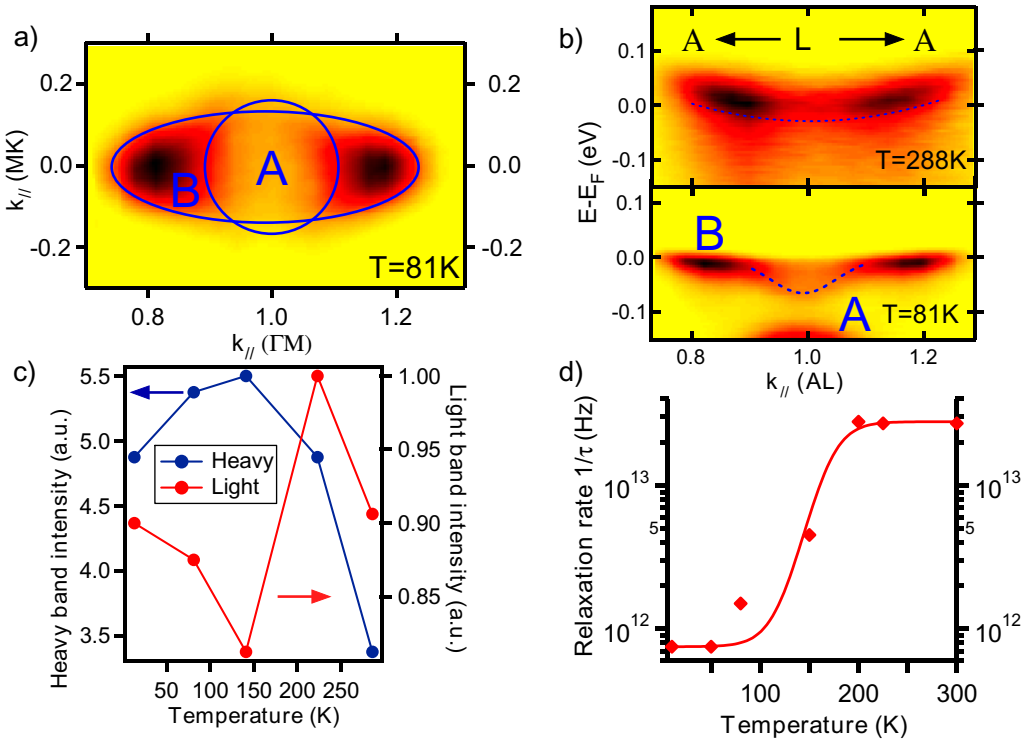


**Figure 13.** (a) Constant energy map of the electron pocket at the Fermi energy and at $L$, showing the typical shape of the main contribution to the FS of $1T$-$TiSe_2$ at LT (here at 81 K). Two characteristic parts are distinguished. (b) Dispersion plots along the long axis of the ellipse to show the drastic mass renormalization of the effective mass. (c) Temperature dependence of the integrated intensity of parts A and B in the partial FS of graph (a). (d) Temperature-dependent relaxation rate in $1T$-$TiSe_2$, obtained from fits to the measured reflectance of Li *et al* [42].

This describes the resistivity of metals arising from charge carriers of density $n$, having an effective mass $m$, which undergo scattering with a relaxation time $\tau$. In the case of $1T$-$TiSe_2$, information about the contribution of holes cannot be easily obtained by means of photoemission, since the top of the valence band suffers a large SW loss. Furthermore, with decreasing temperature, the valence (hole) band at Γ rapidly shifts towards higher binding

energies and disappears from $E_F$. We therefore focus only on the contribution of electrons in the conduction bands, which we have measured and analyzed in detail. Knowing the Drude formula, its parameters can be determined as follows.

- As depicted in figure 13(a), the conduction band can be separated into two parts at LTs, which we call the 'light' and 'heavy' parts. We already obtained their corresponding effective masses previously. Now their relative intensities are estimated. This is done by integrating the SWs at $L$ and $k \simeq 0.85$ AL, respectively, over $\pm 50$ meV around $E_F$, in the same manner as done in our previous study [43]. Indeed, the electron density $n$ of the occupied states in the conduction band can be obtained by

$$n_{V_k} \propto \int_{V_k} \mathrm{d}^3k \int_{-\Delta\omega}^{+\Delta\omega} \mathrm{d}\omega A_c(\vec{k}, \omega) n_F(\omega). \tag{26}$$

  Here $n_F(\omega)$ is the Fermi–Dirac distribution. $A_c(\vec{k}, \omega)$is the spectral function at $L$, which is measured by photoemission. Therefore, limiting the energy integration to the neighborhood of the Fermi energy with $\Delta\omega = 50$ meV permits us to focus on the contribution of the conduction band. Furthermore, restricting the integration in $k$-space over a particular region $V_k$ allows one to focus on a particular contribution. In our case, we restrict ourselves to contributions $A$ and $B$ of the FS to focus on $n_{\mathrm{light}}$ and $n_{\mathrm{heavy}}$. The relative density (of electron type) of the light $n_{\mathrm{light}}$ and heavy $n_{\mathrm{heavy}}$ charge carriers is reproduced in figure 13(c). It is important to keep in mind here that such curves are obtained by comparing the integrated intensities over the *same* regions in $k$-space, where the only parameter changed during the experiment is the temperature. This allows us to say that such curves reflect a change in the probed electron densities, without being affected by photoemission matrix element effects.
- In table 1, the information concerning the effective mass $\tilde{m}_S$ along the short axis of the ellipsoidal electron pocket is incomplete (since the conduction band is close to the Fermi level and at the same time it disperses strongly along the short axis). To give an idea of the resistivity based on the information derived from our photoemission data, we therefore focus on the contributions of the light and heavy charge carriers along the long axis, having the effective masses $\tilde{m}_{L,\mathrm{light}}$ and $\tilde{m}_{L,\mathrm{heavy}}$, respectively.
- In general, the relaxation rate can be estimated from ARPES data using the wave vector width $\Delta k$ of the conduction band at $E_F$ [44]. However, in our case, at high temperatures the centroid of the conduction band does not cross $E_F$, and at LT, the unusual form of the conduction band makes such an analysis clearly difficult and inaccurate. Alternatively, Li *et al* have derived the relaxation rate for the Drude term, which captures the contribution of free carriers (but not that of interband—valence to conduction band—transitions) for $1T$-$TiSe_2$ from optical data [42], but without distinguishing the contribution of holes at $\Gamma$ and electrons at $L$. Due to the differences in the shape of the corresponding FS, we expect their relaxation rates to be different. Figure 13(d) shows their result[13], where holes and electrons are mixed together.

It may be questionable to use the Drude formula, which is established for simple metals, for the case of $1T$-$TiSe_2$, where the conduction band lies above $E_F$ at RT. However, a non-negligible intensity around $E_F$ is present at every temperature and, in our simple approach, it is used as an indication of the charge carrier density $n$.

[13] As a comparison, this relaxation rate at RT has values similar to that of gold [41].

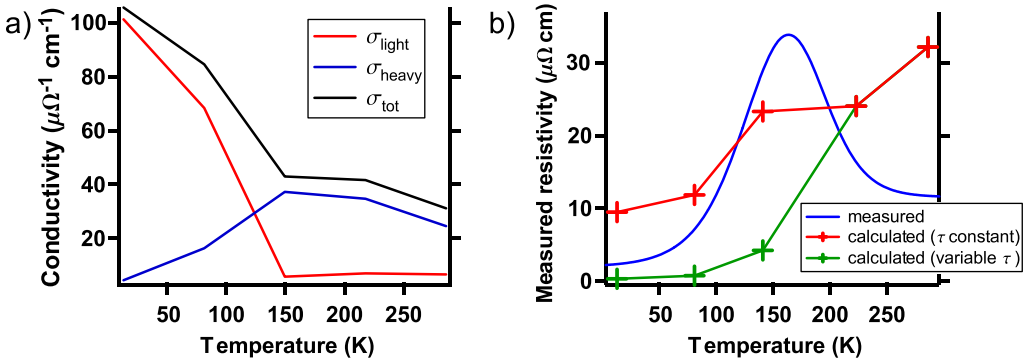


**Figure 14.** (a) Total (black curve) and partial (from the light, red curve, and heavy, blue curve, charge carriers, respectively) conductivities calculated from the integrated intensities and effective masses inferred from ARPES measurements (see text). (b) Calculated resistivity from the total conductivity of graph (a) (red curve) and with additionally a temperature-dependent relaxation rate (green curve), in comparison to the measured one (blue curve). Reprinted from [22]. Copyright 1976, with permission from Elsevier.

Using all these parameters, the conductivity corresponding to the light and heavy charge carriers is computed as a function of temperature (for a constant common relaxation time $\tau$):

$$\sigma = \sigma_{\text{light}} + \sigma_{\text{heavy}} = \frac{n_{\text{light}} e^2 \tau}{m_{\text{light}}} + \frac{n_{\text{heavy}} e^2 \tau}{m_{\text{heavy}}}, \tag{27}$$

first separately as shown in figure 14(a), with the red and blue curves, respectively. In this figure, two regimes are clearly evidenced. At high temperatures, the conductivity is dominated by the numerous heavy carriers, despite their large effective mass. At lower temperatures, whereas the effective mass of the heavy charge carriers increases strongly, quenching their contribution to the conductivity, that of the light charge carriers decreases strongly, enhancing their contribution, which dominates the conductivity.

Then, the resistivity is calculated as the inverse of the total conductivity (black curve in figure 14(a)) and is displayed in figure 14(b) (red curve), together with the measured one (blue line) [22]. We emphasize that only relative values for the charge carrier density $n$ can be derived. Therefore, their absolute value is determined by ensuring visual agreement with the measured resistivity. This gives rise to a RT charge carrier (of electron type) density of $n_{\text{el}} \simeq 0.8 \times 10^{20}\,\text{cm}^{-3}$, which is similar to the value derived by Di Salvo *et al*, $n = 10^{20}\,\text{cm}^{-3}$ [22].

The resistivity calculated with the constant relaxation rate (red curve in figure 14(b)) (which is equal to the RT value of the one obtained in [42]) is increasing over the whole temperature range as a consequence of the two favorable regimes in the conductivity described above. It has a shoulder around 150 K, where the measured resistivity (blue curve) shows its anomaly. However, the number of data points in the resistivity calculated from our photoemission measurements does not allow us to clearly resolve a peak around 150 K. Above 200 K, it still increases, in opposition to the experiment. This discrepancy comes from the fact that the participation of holes at $\Gamma$ is not considered in this calculation. Near RT, despite the presence of electron–hole fluctuations that mimic the effects of the exciton condensate phase and thus open

a gap at Γ, the valence band is sufficiently close to the Fermi energy to provide very light holes (note that $m_v = -0.23m_e$, $m_e$ being the bare electron mass) for conduction. This contribution would therefore strongly enhance the conductivity above $T \simeq 200$ K and decrease the resistivity in this temperature range.

The resistivity calculated with the temperature-dependent relaxation rate from Li *et al* [42] (green curve in figure 14(b)) does not compare well with the experiment, as it is already strongly reduced below 200 K and falls nearly to zero below $T_c$. As explained above, the relaxation rate used in this approach is not fully reliable, because holes and electrons are not distinguished in its derivation. Furthermore, for a (schematical) two-band system with a small gap or overlap like $1T$-$TiSe_2$, we expect that the interband (valence to conduction band) transitions will have a substantial effect on the relaxation rate.

Having different components leading to the resistivity, we are able to relate the upturn and the downturn of the measured curve to particular effects. We associate the major changes happening below $T_c$ with the electron-type charge carrier density variation and in particular to the dramatic reduction of their effective mass, summarized in table 1. Above $T_c$, our analysis suggests that the holes in the valence band at Γ provide the major contribution to transport (in agreement with the Hall resistivity measurement of Di Salvo *et al* [22]) and are mainly suppressed by the gap opening appearing in the CDW phase due to the onset of the exciton condensate phase, causing the resistivity upturn above $T_c$.

However, the influence of the relaxation rate remains unclear and may play a major role. We believe that it should show a marked increase when the temperature approaches $T_c$ from higher values, in answer to the interband scattering channel offered by the electron–hole fluctuations evidenced in our photoemission measurements. This scattering channel would disappear progressively below $T_c$, when the exciton condensate is well established and when fluctuations decrease, so that the scattering rate should decrease again. At the same time, the soft phonon mode observed at $T_c$ [24] is also expected to strongly contribute to a relaxation rate increase around this temperature. Furthermore, the disappearance of the hole pocket at Γ certainly leads to a drastic change of the relaxation rate. A detailed calculation (e.g. via the Boltzmann equation) taking into account the FS topology, the electron–hole fluctuations and the soft phonon mode is necessary to clarify the situation.

## 8. Conclusion

We have shown recent ARPES results on $1T$-$TiSe_2$, which we interpret in the framework of the exciton condensate phase model. Calculation of the spectral function from this model allows us to compute photoemission intensity maps, which compare well with the experiment, supporting strongly this mechanism as the origin of the CDW phase of $1T$-$TiSe_2$. The temperature dependence of the corresponding order parameter is extracted from photoemission measurements, together with a substantial chemical potential shift. The order parameter reaches values above 100 meV at LT, pointing towards a strong coupling between electrons and holes below $T_c$. It also suggests that intense electron–hole fluctuations are already present above $T_c$, anticipating the exciton condensation. All these elements give us a deeper understanding of the possible realization of the exciton condensate phase. Finally, the transport properties of $1T$-$TiSe_2$ are addressed with this knowledge, and basic ingredients leading to the anomalous resistivity of this system are suggested.

However, as outlined in section 5.3, *direct* evidence of the exciton condensate at LT in $1T$-$TiSe_2$, is still lacking; it could prove unambiguously the existence of this exotic phase. We hope that this work will stimulate other studies that will possibly find this *direct* evidence.

## References


[1] Keldysh L V and Kopaev Y V 1965 Possible instability of semimetallic state toward Coulomb interaction *Sov. Phys.—Solid State, USSR* **6** 2219

[2] Jérome D, Rice T M and Kohn W 1967 Excitonic insulator *Phys. Rev.* **158** 462–75

[3] Doni E and Girlanda R 1986 *Electronic Structure and Electronic Transition in Layered Materials* (Dordrecht: Reidel)

[4] Cui X Y, Negishi H, Titov A N, Titova S G, Shi M and Patthey L 2010 Evolution of electronic structure on transition metal doped titanium disulfide by angle resolved photoemission spectroscopy study arXiv:1008.1146v1

[5] Cercellier H *et al* 2007 Evidence for an excitonic insulator phase in $1T$-$TiSe_2$ *Phys. Rev. Lett.* **99** 146403

[6] Rasch J C E, Stemmler T, Müller B, Dudy L and Manzke R 2008 $1T$-$TiSe_2$: semimetal or semiconductor? *Phys. Rev. Lett.* **101** 237602

[7] Rossnagel K, Kipp L and Skibowski M 2002 Charge-density-wave phase transition in $1T$-$TiSe_2$: excitonic insulator versus band-type Jahn–Teller mechanism *Phys. Rev.* B **65** 235101

[8] Kidd T E, Miller T, Chou M Y and Chiang T-C 2002 Electron–hole coupling and the charge density wave transition in $TiSe_2$ *Phys. Rev. Lett.* **88** 226402

[9] Claessen R *et al* 1996 Complete band-structure determination of the quasi-two-dimensional Fermi-liquid reference compound $TiTe_2$ *Phys. Rev.* B **54** 2453–65

[10] Clerc F *et al* 2004 Spin–orbit splitting in the valence bands of $1T$-$TaS_2$ and $1T$-$TaSe_2$ *J. Phys.: Condens. Matter* **16** 3271

[11] Vernes A, Ebert H, Bensch W, Heid W and Näther C 1998 Crystal structure, electrical properties and electronic band structure of tantalum ditelluride *J. Phys.: Condens. Matter* **10** 761

[12] Yoshida Y and Motizuki K 1980 Electron lattice interaction and lattice instability of $1T$-$TiSe_2$ *J. Phys. Soc. Japan* **49** 898

[13] Wilson J A and Mahajan S 1977 The anomalous behaviour of $TiSe_2$ and the excitonic insulator mechanism *Commun. Phys.* **2** 23

[14] Wilson J A 1978 Modelling the contrasting semimetallic characters of $TiS_2$ and $TiSe_2$ *Phys. Status. Solidi* B **86** 11

[15] Monney C *et al* 2009 Spontaneous exciton condensation in $1T$-$TiSe_2$: BCS-like approach *Phys. Rev.* B **79** 045116

[16] Zhitomirsky M E and Rice T M 2000 Electron–hole liquid in the hexaborides *Phys. Rev.* B **62** 1492–5

[17] Wachter P, Bucher B and Malar J 2004 Possibility of a superfluid phase in a Bose condensed excitonic state *Phys. Rev.* B **69** 094502

[18] Bronold F X and Fehske H 2006 Possibility of an excitonic insulator at the semiconductor–semimetal transition *Phys. Rev.* B **74** 165107

[19] Ihle D, Pfafferott M, Burovski E, Bronold F X and Fehske H 2008 Bound state formation and the nature of the excitonic insulator phase in the extended Falicov–Kimball model *Phys. Rev.* B **78** 193103

[20] Zenker B, Ihle D, Bronold F X and Fehske H 2010 Existence of excitonic insulator phase in the extended Falicov–Kimball model: SO(2)-invariant slave-boson approach *Phys. Rev.* B **81** 115122

[21] Phan N P, Becker K W and Fehske H 2010 Spectral signatures of the BCS–BEC crossover in the excitonic insulator phase of the extended Falicov–Kimball model *Phys. Rev.* B **81** 205117

[22] Di Salvo F J, Moncton D E and Waszczak J V 1976 Electronic properties and superlattice formation in the semimetal $TiSe_2$ *Phys. Rev.* B **14** 4321–28

[23] Levy F and Froideveaux Y 1979 Structural and electrical properties of layered transition-metal selenides $V_xTi_{1-x}Se_2$ and $Ta_xTi_{1-x}Se_2$ *J. Phys. C: Solid State Phys.* **12** 473–87
[24] Holt M, Zschack P, Hong H, Chou M Y and Chiang T-C 2001 X-ray studies of phonon softening in $TiSe_2$ *Phys. Rev. Lett.* **86** 3799–802
[25] Hughes H P 1977 Structural distortion in $TiSe_2$ and related materials—possible Jahn–Teller effect *J. Phys. C: Solid State Phys.* **10** L319–23
[26] Zunger A and Freeman A J 1978 Band structure and lattice instability of $TiSe_2$ *Phys. Rev. B* **17** 1839–42
[27] van Wezel J, Nahai-Williamson P and Saxena S S 2010 Exciton–phonon-driven charge density wave in $TiSe_2$ *Phys. Rev.* B **81** 165109
[28] Morosan E, Zandbergen H W, Dennis B S, Bos J W G, Onose Y, Klimczuk T, Ramirez A P, Ong N P and Cava R J 2006 Superconductivity in $Cu_xTiSe_2$ *Nature Phys.* **2** 544–50
[29] Sawatzky G A, Elfimov I S, van den Brink J and Zaanen J 2009 Heavy-anion solvation of polarity fluctuations in pnictides *Europhys. Lett.* **86** 17006
[30] Kusmartseva A F, Sipos B, Berger H, Forró L and Tutiš E 2009 Pressure induced superconductivity in pristine $1T$-$TiSe_2$ *Phys. Rev. Lett.* **103** 236401
[31] Mahan G D 1981 *Many-Particle Physics* (New York: Plenum)
[32] Clerc F 2006 Photoemission from transition metal dichalcogenides quasi-two dimensional systems with charge density waves *PhD Thesis* University of Neuchâtel, Switzerland
[33] Caillé A, Lepine Y, Jericho M H and Simpson A M 1983 Thermal expansion, ultrasonic velocity, and attenuation measurements in $TiS_2$, $TiSe_2$, and $TiS_{0.5}Se_{1.5}$ *Phys. Rev.* B **28** 5454–61
[34] Woo K C, Brown F C, McMillan W L, Miller R J, Schaffman M J and Sears M P 1976 Superlattice formation in titanium diselenide *Phys. Rev.* B **14** 3242–47
[35] van Wezel J, Nahai-Williamson P and Saxena S S 2010 An alternative interpretation of recent ARPES measurements on $TiSe_2$ *Europhys. Lett.* **89** 47004
[36] Voit J, Perfetti L, Zwick F, Berger H, Margaritondo G, Grner G, Hchst H and Grioni M 2000 Electronic structure of solids with competing periodic potentials *Science* **290** 501
[37] Clerc F, Battaglia C, Cercellier H, Monney C, Berger H, Despont L, Garnier M G and Aebi P 2007 Fermi surface of layered compounds and bulk charge density wave systems *J. Phys.: Condens. Matter* **19** 355002
[38] Hengsberger M, Purdie D, Segovia P, Garnier M and Baer Y 1999 Photoemission study of a strongly coupled electron–phonon system *Phys. Rev. Lett.* **83** 592–5
[39] Pillo Th, Hayoz J, Berger H, Lévy F, Schlapbach L and Aebi P 2000 Photoemission of bands above the Fermi level: the excitonic insulator phase transition in $1T$-$TiSe_2$ *Phys. Rev.* B **61** 16213–22
[40] Monney C *et al* 2009 Dramatic effective mass reduction driven by strong electronic correlations arXiv:0912.5283
[41] Ashcroft N W and Mermin N D 1976 *Solid State Physics* (London: Brooks and Cole)
[42] Li G, Hu W Z, Qian D, Hsieh D, Hasan M Z, Morosan E, Cava R J and Wang N L 2007 Semimetal-to-semimetal charge density wave transition in $1T$-$TiSe_2$ *Phys. Rev. Lett.* **99** 027404
[43] Monney C, Schwier E F, Garnier M G, Mariotti N, Didiot C, Beck H, Aebi P, Cercellier H, Marcus J, Battaglia C, Berger H and Titov A N 2010 Temperature-dependent photoemission on $1T$-$TiSe_2$: interpretation within the exciton condensate phase model *Phys. Rev.* B **81** 155104
[44] Yoshida T *et al* 2003 Metallic behavior of lightly doped $La_{2-x}Sr_xCuO_4$ with a Fermi surface forming an arc *Phys. Rev. Lett.* **91** 027001